UNIVERSITY
OF LATVIA

Summary
of Doctoral Thesis

Didzis Berenis

NUMERICAL SIMULATION OF ROTATING PERMANENT MAGNET INDUCED TURBULENT LIQUID METAL FLOW

Riga 2023

UNIVERSITY
OF LATVIA

FACULTY OF PHYSICS, MATHEMATICS AND OPTOMETRY

Didzis Berenis

Numerical simulation of rotating permanent magnet induced turbulent liquid metal flow

SUMMARY OF DOCTORAL THESIS

Submitted for the degree of Doctor of physics
Subfield: fluid mechanics

Scientific supervisor:
Dr. phys. Ilmārs Grants

Rīga, 2023

The doctoral thesis was carried out at the Institute of Physics, MHD Technology laboratory, University of Latvia, from 2018 to 2023.

NATIONAL
DEVELOPMENT
PLAN 2020

EUROPEAN UNION
European Regional
Development Fund

INVESTING IN YOUR FUTURE

UNIVERSITY OF LATVIA
FOUNDATION

The doctoral thesis contains four scientific publications.
Form of the doctoral thesis: collection of publications in Physics and Astronomy, subfield of fluid mechanics.

Supervisor: Dr. phys. Ilmārs Grants, leading researcher of MHD Technology laboratory at the Institute of Physics, University of Latvia.

Reviewers:

1. Dr. phys. Andris Jakovičs, University of Latvia;
2. Dr. Valdis Bojarevičs, University of Greenwich, United Kingdom;
3. Dr. Bernard Nacke, Leibniz University Hannover, Germany.

The thesis will be defended at the public session of the Doctoral Committee of physics, University of Latvia, at 13:00 on June 2, 2023.

The thesis is available at the Library of the University of Latvia, Kalpaka boulevard 4.

Chairman of the Doctoral Committee	Dr. phys. Andris Jakovičs
Secretary of the Doctoral Committee	Sintija Siliņa

ISBN 978-9934-18-987-6
ISBN 978-9934-18-988-3 (PDF)

Abstract

This thesis is devoted to numerical and experimental study of a rotating permanent magnet (RPM) generated turbulent flow of an electrically-conducting liquid in a closed volume. A setup of axially symmetric liquid container with coaxial transversely magnetized cylindrical RPM is considered. Alternating magnetic field of an RPM induces electrical currents and, thus, electromagnetic (EM) body force in the nearby conductor. An analytical solution in a form of infinite series involving elliptic integrals is obtained for the force created by a co-axial cylindrical RPM in a conducting cylinder or a cylindrical ring. The solution is compared to an experiment as well as numerical simulation results. A simplified analytical solution is then obtained for the RPM-driven turbulent flow in a cylinder. For this purpose the effect of radial dependency of the driving force is incorporated in an existing similarity solution. This solution allows to estimate the maximum flow velocity as well as radial position of the maximum. It also offers an explanation of a counter-intuitive axial position of the velocity maximum in the opposite side of the liquid cylinder with respect to the RPM. Turbulent flow is computed numerically in a cylinder by combining open source simulation programs *OpenFOAM* and *Elmer*. A method is developed to account for ferromagnetic parts intended to enhance the EM body force. Results of analytical and numerical solution are compared to measurements in a low temperature liquid metal experiment. The good agreement by different approaches in this particular case is not warranted generally as illustrated by another configuration considered next. Instability of flow is studied numerically in a ring channel driven by RPM in its center, where a free shear radial jet develops in a wide ring configuration. The first instability produces two new steady axially symmetric solutions with the jet shifted upwards or downwards. As the RPM-induced force magnitude increases the jet becomes periodic and, ultimately, fluctuating irregularly. Concurrently the jet is distinctly shifted from the axial mid-plane on average. This is followed by a state of turbulent bistability when the jet randomly switches between leaning up or down. Flow having more than one time-average state poses fundamental difficulties for turbulence models which use the description of a single time-average. This may explain sometimes poor agreement between measurements and standard turbulence models applied to closed EM driven flows. Turbulent bistability emerges in the considered case at a low Reynolds number. This offers a convenient model case for development of techniques to predict the phenomenon. An experiment was set up to observe bistability in a transparent electrolyte ring, where dye wakes were visually observed over time span of several hours. Long-living flow states were observed but the experimental evidence of bistability was not as compelling as in the corresponding numerical simulation.

Acknowledgements

Foremost, I express my gratitude to my thesis supervisor Dr. Ilmārs Grants for the given opportunity, the time devoted and the successful communication throughout the development of the thesis.

I appreciate the advice of Valters Dzelme on using programs *OpenFOAM* and *Elmer*. I thank Antra Gaile for help with measurements that helped to validate analytical force model and thank Matīss Kalvāns for the advice and help on constructing the measurement setup. I am thankful to Reinis Baranovskis for sharing experimentally measured velocity data for the comparison with numerical calculations.

Furthermore, I am grateful to Kalvis Kalniņš, Raimonds Nikoluškins and Ingus Pagasts for the help in preparing experimental setup that allowed to observe flow fluctuations in electrolyte flow. I also thank Ivars Krastiņš for numerous discussions on various software related questions. Additionally I thank all my colleagues from the MHD Technology Laboratory at the Institute of Physics for the productive atmosphere and positive mindset.

Sincerest thanks to my wife Dace for the patience, support and understanding.

I highly appreciate being financially supported during the thesis development by the grant from SIA “Mikrotikls” – the patron of University of Latvia Foundation.

Contents

Introduction

Rotating permanent magnet use for flow generation

A rotating permanent magnet (RPM) is an efficient means for generating electrically conducting liquid flow without contact. An alternating magnetic field due to the magnet rotation causes a time-averaged body force in the nearby conductor. This method has long been applied in metallurgy [1, 2], crystal growth [3, 4, 5], and other technologies using electromagnetic (EM) induction with magnetic field inductors. Replacing the magnetic field inductors with an RPM avoids Joule heat losses associated with magnetic field generation. Advantage of permanent magnets (PMs) is also the simplicity of device construction. Early PMs were too weak to materialize this idea in working applications, but since the advent of rare-earth PMs it was possible to build liquid metal pumps, first proof-of-concept devices built at Institute of Physics of University of Latvia (IPUL) in mid-1990s [6]. Later PM pumps were developed for industrial partners and scientific institutions [7, 8, 9]. Since then, efficient PM stirrers have been built as well [10] (Zmag, see https://www.zmag.net/). As the use of RPM systems is relatively new, their other potential applications can be expected and explored. For example, preliminary studies have already been conducted on RPMs designed as centrifugal pumps for low-temperature melts [11, 12].

In the IPUL an innovative method has been developed for stirring electrically conductive liquids with RPMs. This method can also be used for pumping electrically conducting liquids and it differs from traditional RPM pumps. There is a large freedom in the design of a stirrer and pump but each change affects the performance of the device: efficiency, maximum velocity, flow distribution etc. The problem involves academic questions about multi-physical problem, answers to which will increase the scope of solved numerical hydrodynamics tasks. At the same time, the problem is closely related to the design of industrial devices and the solution will open possibility to do engineering calculations for physically complicated devices that have large value in industry but are theoretically not fully understood yet. The experiments and calculations done previously justify this method to be superior over now widely used EM stirring method. However, the theoretical understanding of this problem is not sufficient to develop stirrer with a predictable generated flow.

Rotating magnetic field (RMF) driven flows are known to develop quasi solid-body rotating core [1] with little effect of azimuthal force distribution. Moreover, the rotation tends to dominate even if the radial or axial forces are comparable [13]. These general properties allow to make reasonable predictions of the RPM driven flow in cylindrical enclosures based upon the integral magnetic torque. In RPM stirrer and pump setups, however, sometimes time-averaged turbulence models and experimental measurements are in strong disagreement and a conclusive reason for error is not found. In symmetric RPM systems time-averaged numerical simulations predict symmetric turbulent velocity distribution [14], whereas experimental measurements show flow asymmetry [14, 15]. Perhaps in some cases this discrepancy can be attributed to experimental error. At the same time, experiments show low frequency dynamics [16, 15], the presence of which could lead to difficulties for time-averaged turbulence models and eventually calculation errors. This phenomena is very little studied numerically and theoretically. Finding conclusions to questions involving RPM stirrer and pump setup involves development of numerical simulation methods which have academic value and could be adapted for solving other tasks that involve electrically conductive liquid flows.

With the currently available numerical modelling techniques it is not possible to perform a calculation so extensive to include all the construction variations (ways to affect the flow); therefore, it is difficult to find the optimal solution for a given industrial task. Similarly, academic questions about RPM systems are difficult to answer. It can be difficult to find numerical tools that for all system regimes can answer to a fundamental question of the study: what is the distribution of the RPM induced current and the generated turbulent flow, which is generated by the magnetic forces? The RPM generated flow of poor conductors, such as, electrolytes, usually can not reach velocities that are comparable with the velocity of the RMF. Then mathematically questions about RPM induced currents are linear. Solution is additionally simplified if the RPM generated currents are not strong enough to generate a secondary magnetic field, which significantly disturbs the current distribution.

In contrast, RPM generated liquid metal flow can reach velocities comparable to RMF velocity, in which case conducting liquid velocity distribution significantly affects the total current density distribution and the problem is non-linear. Still, neglecting velocity in current density calculation can often serve as an initial approximation and the current density correction due to velocity distribution can be introduced later. Additionally, the RPM stirrer and pump systems are in small magnetic Reynolds number (Re_m) regimes, which ensures insignificant magnetic field generation from the velocity distribution. Small Re_m regimes infers that EM and hydrodynamic equation systems can be solved separately. As a result, large part of the objective of the study, which is in the RPM system relevant parameter range, can be solved analytically. Such solutions, however, are not yet available in the scientific literature because the physical setup is rather new.

Literature survey

Analytical expression of the magnetic field created by a cylindrical transversely magnetized PM has been recently published [17]. However, a corresponding expression for the induced currents and magnetic forces has not been produced. An analytical volume force expression has proven useful in case of a uniform RMF [18] for many upcoming flow studies [19, 4, 20, 21]. Axially symmetric geometries are often used for EM stirrers and pumps. One of which is a shallow cylinder or disc because it has a large axial boundary surface area. Applying azimuthally non-uniform axial magnetic field with an angular rotational frequency introduces azimuthal velocity of the liquid metal in the channel and a strong outward radial pressure is generated [7]. This type of setup is used in centrifugal pumps [7], where the relatively large cross section of the channel provides an efficient way of generating large flow rates. However, for disc type pumps the thickness of outer radial wall needs to be reinforced to withstand the high pressure conditions at large flow rates [7]. On the other hand, thin cylindrical channel or ring configurations can safely operate at higher flow rates with smaller wall thickness [7].

The two types of setups – disc or ring configuration – has been considered for EM induced liquid metal stirring or mass transport in large baths of melt [12, 22, 23]. The potential applications include temperature homogenization and scrap metal mixing with the melt in aluminium remelting furnaces [10], micro and nano particle dispersion of agglomerates and mixing with metal [24, 25], degassing of aluminium, and liquid metal transport for aluminium dispenser [26]. RPM generated flows have been studied for various industrial applications, such as, liquid metal transport [6], melt mixing in aluminum furnaces [10], particle mixing with metal for composite material production [27, 28].

Usually EM induced liquid metal flows are highly turbulent and it is not possible to perform a direct numerical calculation (DNS) in a practical time scale. Then, turbulence modelling, which reduces the necessity to distinguish all of the details of the flow, can be used. Popular because of the quick calculation times is a class of turbulence models called Reynolds averaged Navier–Stokes (RANS). The assumption of RANS models is that the flow can be separated in the time-averaged part and the turbulent velocity fluctuations. RANS models are in good agreement with experiments for systems where the model assumptions are reasonably fulfilled. For example, flow in a pipe [29, 30], swirling flow in a cylinder [1, 31], and jet flow [32].

Sometimes flows are more complicated and multiple competing solutions exist, which might be a problem for time-averaged description [14, 16, 15, 33, 34, 35]. In such cases problems might be caused by bifurcating solutions. A simple example of bifurcation – pitchfork bifurcation – is when a bifurcation of a stationary solution occurs and multiple new solutions emerge from which only one manifests. Another type of bifurcation – Hopf bifurcation [36] – describes the transition from steady state to cyclic solution. Additionally, a hysteresis loop can form near Hopf bifurcation [37]. At certain system parameters the system can become aperiodic or intermittent. This transition to chaos is usually referred to as the Pomeau–Manneville scenario [38]. The chaotic regimes have been sorted in several categories [39, 40, 41]. One kind of regime known as on–off intermittency [42] has a characteristic occasional bursts (the "on" state) that allow transition to the other system attractor, in which the system can spend long time intervals (referred to as the "off" state) before another transition occurs. The time spent in either position is random and can exceed the characteristic momentum diffusion time. System can exhibit on–off intermittency even if there is only one stable attractor. However, if the system has another attractor to which the system can transition during one of the bursting events, then the phenomenon is called two-state on–off intermittency [43].

A signature statistical behaviour, which helps to identify the on–off intermittent systems are the "off" state intervals following $-3/2$ slopes in log–log scale [44, 45, 46]. The characteristics of on–off intermittency have been determined in various fluid dynamics systems, such as in the wake behind an obstacle [47, 48, 49, 50], drift waves [51], spherical Couette flow [52], and liquid-metal flow in a magnetic field [53]. The phenomenon of transitioning between regimes has also been observed in neural activity. For example, the characteristic patterns of on–off intermittency is observed in recorded intervals between epileptic seizures in mouse brains [45] and also in a human task of balancing a stick on a fingertip [54]. The phenomenon of on–off intermittency may play a role in explaining observed geodynamo and solar activity. The sequence of reversals of the Earth's magnetic field bears some semblance to on–off intermittent behavior [55, 56, 57]. It is difficult to analyze such a complicated system as geodynamo alone [58] and even more so if external factors are considered. This naturally leads to the question: are the reversals of the Earth's magnetic field due to internal or external factors, e.g., solar activity [59]? Solar activity has been attributed to on–off intermittent behavior [60, 59]. However, the underlying mechanism of solar cycles being externally forced or internally generated is being actively debated [61, 62]. There are a few questions that are common to all of the above mentioned systems: are external factors necessary to initiate the transition, what is causing this transition, and can the transitions be predicted?

DNS of multiple long-lived "off" states is not feasible in large Reynolds number (Re) regimes. Calculation in large Re regimes is possible with large eddy simulation turbulence models [49], but it is impractical for parametric studies. On the other hand, mean field turbulence models in the presence of on–off intermittency are problematic and can provide skewed results. One method could be to identify and find the mean of each of the "off" states, which has been studied using similar approach and by reducing the dimensions of the system

[50]. A set of open-access numerical tools that could help to answer questions about RPM stirrer systems are *Elmer* (http://www.elmerfem.org/), *OpenFOAM* (https://openfoam.org/), and *EOF-Library* [63]. RPM induced current density and volume force distribution in conducting bodies can be obtained using Elmer. Given that the volume force is provided, the generated flow can be obtained using software *OpenFOAM*, where the software *EOF-Library* provides the communication back and forth between *Elmer* and *OpenFOAM*.

Aim and objectives of the thesis

The main goal of the doctoral thesis is to numerically study RPM stirred electro-conducting liquid flow and seek explanations for sometimes obtained major disagreements between experimental measurements and time-averaged turbulence models. The main objectives of the study are:

- to develop solvers for calculating RPM generated volume force and the resulting turbulent flow in simple geometries;
- to obtain RPM induced volume force distribution in an electrically-conducting sample;
- to calculate RPM generated turbulent flow distribution in various liquid container geometries;
- to evaluate the time-averaged model performance for the flow description.

Contribution of the author

Author has derived analytical solution in a form of infinite series involving elliptic integrals for volume force created by a co-axial cylindrical RPM in a conducting cylinder or a cylindrical ring [dis1]. To complement the analytical solution, author prepared experimental setup and measured the force experimentally [dis1]. Author obtained a simplified analytical solution for the RPM-driven turbulent flow in a cylinder [dis2], and also computed the turbulent flow numerically [dis2]. Additionally, author developed a method to account for ferromagnetic parts intended to enhance the EM body force [dis2]. Author has performed numerous calculations with *OpenFOAM* to investigate the instability of flow in a ring channel driven by an RPM in its center. The calculations were performed as a part of parametric sweep by varying geometry [dis3] or by varying the force parameter [dis4]. Additionally, author performed numerical calculations to investigate the bi-stable nature of the flow. Furthermore, author developed, tested and improved experimental setup through several iterations that eventually allowed for experimental observation of the flow direction change in a ring setup of a transparent electrolyte [dis4].

Structure of the thesis

In this work, systems where RPM induces force in containers filled with liquid conductor are studied. The analytical description of the induced volume force, which is derived for axi-symmetric configurations with a co-axial RPM, is described in chapter 1 and explained in detail in the article [dis1]. The generated flow in one of such configurations – a cylindrical container placed above a RPM – is studied in detail in [dis2]. The main results of this study are presented in chapter 2. Another type of axi-symmetric configuration is ring-shaped container which is placed around a RPM. The flow stability dependence on the ring outer radius was studied in [dis3] and the chaotic nature of the flow in [dis4]. The results of these studies are presented in chapter 3.

Approbation of results

Published papers

[dis1] D. Berenis, I. Grants, "Analytical induced force solution in conducting cylindrical bodies and rings due to a rotating finite permanent magnet", *Journal of Magnetism and Magnetic Materials*, Volume 497, 165856 (2020), https://doi.org/10.1016/j.jmmm.2019.165856

[dis2] D. Berenis, R. Baranovskis, I. Grants, T. Beinerts, and A. Bojarevičs, "Permanent magnet bottom-stirred swirling flow in coaxial shallow cylindrical containers", *Physics of Fluids* 33, 055127 (2021), https://doi.org/10.1063/5.0047706

[dis3] I. Grants, D. Berenis, "Stability of electrically conducting liquid flow driven by a rotating magnetic dipole in a ring channel", *Physics of Fluids* 32, 044104 (2020), https://doi.org/10.1063/5.0002094

[dis4] D. Berenis, I. Grants, "Experimental and numerical investigation of bistability in rotating permanent magnet-generated electrolyte flow in a ring-shaped container", *Physics of Fluids* 34, 124106 (2022), https://doi.org/10.1063/5.0128454

Published papers that are not included in the thesis:

[dis5] K.K. Berga, D. Berenis, M. Kalvāns, et al. "Model Experiment for Molten Metal Temperature Homogenization with Rotating Permanent Magnet", *JOM* 74, 2450–2460 (2022), https://doi.org/10.1007/s11837-022-05288-y

[dis6] R. Baranovskis, D. Berenis, I. Grants, et al. “Contactless Aluminum Degassing System—GaInSn Model Experiments and Numerical Study”, *J. Sustain. Metall.* 7, 1899–1909 (2021), https://doi.org/10.1007/s40831-021-00459-8

Participation in conferences

Results have been presented at international scientific conferences:

[conf1] D. Berenis, I. Grants, “Numerical simulations on bifurcations and experiments on bi-stability in forced transparent electrolyte flow in a ring-shaped container”, BIFD 2022, August 17, 2022, Groningen, Netherlands

[conf2] D. Berenis, I. Grants, “Experiments on bi-stability in rotating permanent magnet generated electrolyte flow in a ring-shaped container”, PAMIR 2022, July 5, Krakow, Poland

[conf3] D. Berenis, I. Grants, “Transition to turbulence of electrically conducting liquid flow driven by a rotating magnetic dipole in a ring channel”, 25th International Congress of Theoretical and Applied Mechanics, Thematic Session – Flow Instability and Transition, August 27, 2021

[conf4] D. Berenis, I. Grants, “Analytical solution of electromagnetic force and numerical calculation of the flow in a conducting cylindrical ring due to a rotating permanent magnet”, 11th pamir International Conference Fundamental and Applied MHD, July 4, 2019, Reims, France

And at the annual conferences of the University of Latvia:

[conf5] D. Berenis, I. Grants, T. Beinerts, A. Bojarevičs, “Bi-stable turbulence of forced liquid metal flow in a rectangular container”, 80th Latvijas Universitātes zinātniskā konference, 04.02.2022, Riga, Latvia

[conf6] D. Berenis, I. Grants, “Rotējošu pastāvīgo magnētu inducētā spēka analītisks atrisinājums elektrovadošos gredzenos”, 77th Latvijas Universitātes starptautiskā zinātniskā konference, sekcija Fundamentālā un lietišķā magnetohidrodinamika, 22.02.2019, Riga, Latvia

Participation in scientific projects

- Implementation of activities described in the Roadmap to Fusion during Horizon Europe through a Joint Programme of the members of the EUROfusion consortium under Horizon Europe/WP24-TRED (Apmācība un izglītība: kvalifikācijas darbu sagatavošana)

- "LU doktorantūras kapacitātes stiprināšana jaunā doktorantūras modeļa ietvarā", Nr. 8.2.2.0/20/I/006

- Jauna tipa bezkontakta elektromagnētiskas vieglo sakausējumu degazācijas sistēmas izstrāde (Rūpnieciskie pētījumi), reģ. Nr. 1.1.1.1/18/A/149

- Magnetohidrodinamisko nestabilitāšu izpēte liela mēroga šķidro metālu bateriju realizācijai, reģ. Nr. lzp-2018/1-0017

- Combined CPS and fast moving liquid metal free surface for large power applications in divertor Description (WP8, WPDTT1, Porainās vides un materiāli)/EUROFUSION project "Implementation of activities described in the Roadmap to Fusion during Horizon 2020 through a Joint programme of the members of the EUROfusion consortium" (akronīms- EUROfusion)

- Līgums par zinātniski tehniskās produkcijas sagatavošanu un zinātniski tehniskā pakalpojuma sniegšanu projekta "Tehnoloģijas izstrāde silīcija rūpniecības atkritumu pārstrādei par silīcija-alumīnija ligatūru" vajadzībām, reģ. Nr. EPM-2015-1

1. Model description and analytical volume force

The considered geometry of the model is axially symmetric, where the transversely magnetized cylindrical PM with remanent magnetization B_{rem} and radius r_m is placed on the axis of symmetry and rotating with angular frequency ω. In Fig. 2 we have illustrated our axially symmetric model for a conducting ring with arbitrary axial and radial boundaries, where r is the radial and z is the axial direction. In top view (Fig. 2a) we have shown $r_i,\ r_o$ – the inner and outer radius of the conducting body. And in side view (Fig. 2b) are shown geometrical parameters h_m – the half height of the magnet and $z_1,\ z_2$ – bottom and top boundaries of the conducting body. The density and electrical conductivity of the conducting ring is ρ and σ, respectively. The scope of the model also includes cylindrical conducting bodies ($r_i = 0$) when $z_1 > h_m$ or $z_2 < -h_m$.

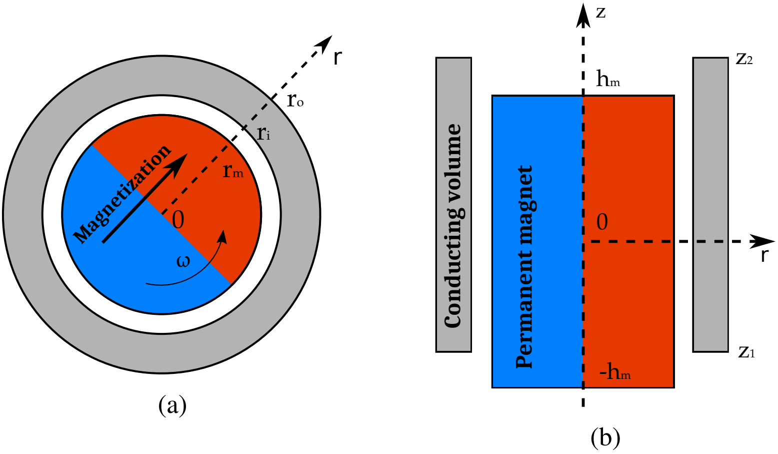

Figure 2. Sketch of the model:(a) horizontal cross-section of the model; (b) vertical cross-section through the cylinder axis.

The RPM induces currents in the conducting body which, in combination with magnetic field, gives rise to volume force. The volume force is $\mathbf{F} = \mathbf{J} \times \mathbf{B}$ – the cross product of the induced current density, $\mathbf{J}$, and the magnetic flux density, $\mathbf{B}$. The RPM in-a-contactless-manner-generated electrically conducting liquid velocity, $\mathbf{u}$, can be determined by solving incompressible Navier–Stokes (N–S) equation

$$\rho\left(\frac{\partial \mathbf{u}}{\partial t} + \mathbf{u}\cdot\nabla\mathbf{u}\right) = \nu\nabla^2\mathbf{u} - \nabla p + \mathbf{F}, \tag{1}$$

where p is pressure.

RPM stirrers for electrically conducting liquids usually have common conditions that can be expressed through nondimensional parameters.

Characteristic quantities (Table 1) L, T, and B set the scales for J, U, and P. Following dimensional analysis, scales for all the other quantities used in our model can be obtained as well.

Quantity	*Symbol*	*Definition*
Length	L	
Time	T	
Magnetic flux density	B	
Current density	J	$\omega\sigma BL$
Velocity	U	ν/L
Pressure	P	ρU^2

Table 1. Definitions of quantities used for nondimensionalization.

The general approach for calculating EM-stirred (or with RPMs) liquid melt flow usually takes into account skin-effect and velocity distribution of the liquid conductor.

The conducting liquid volume velocity distribution can be expressed in a dimensionless form as $\mathbf{v} = \mathbf{u}/U$. The characteristic velocity is usually an unknown, so Reynolds number is defined as the maximum dimensionless velocity $Re = \max|\mathbf{v}|$ of the conducting body. To characterize the RPM generated velocity of the magnetic field, the Reynolds number of the RMF is defined as $Re_\omega = \omega L/U$. If the characteristic velocity $Re/Re_\omega \ll 1$, then velocity of the conducting body can be neglected in the current density generation.

Skin-effect can be neglected if the dimensionless frequency, $S = Pr_m Re_\omega$, satisfies the condition $S \leq 3$ [1]. Here, magnetic Prandtl number is defined as $Pr_m = \nu\sigma\mu_0$, where μ_0 is the permeability of vacuum. For most common liquid conductors, including liquid metals, Pr_m is very small ($Pr_m < 10^{-5}$), so the condition $S \leq 3$ is satisfied unless Re_ω is very large.

Magnetic Reynolds number can be expressed through the introduced definitions $Re_m = RePr_m$ and is also assumed to be negligible ($Re_m \ll 1$), which provides that velocity of the conducting volume does not contribute to the magnetic field generation. The induced body force has a time-averaged part, $\langle\mathbf{F}\rangle$, and an oscillatory part. In our investigation we assume that the inertia of the fluid is large enough to neglect the oscillatory component of the force. This can be characterized by requiring the magnetic interaction parameter, $N = Ha^2/Re_\omega$, to be small ($N \ll 1$). Here, Hartmann number $Ha = BL\sqrt{\sigma/\nu\rho}$ is the dimensionless measure of magnetic field strength.

Such parameter range is common in certain applications (particularly the semiconductor crystal growth). The assumptions $S \leq 3$, $Re_m \ll 1$, and $N \ll 1$ are often fulfilled also for liquid metal stirring applications. However,

$Re/Re_\omega \ll 1$ is usually not fulfilled and velocity of the liquid metal must be taken into account in the induced current density calculation.

Allowing for some error, we can determine the correction coefficient by assuming rigid-body rotation. The corrected angular velocity is found by determining the slip correction

$$\Omega_1 = \frac{\Omega_0}{1+\Omega_0/\omega}, \tag{2}$$

where $\Omega_0 = Re\ U/L$ is the calculated angular velocity without the slip correction.

1.1. RPM induced volume force derivation

In the volume force derivation we look at the simple case of conducting solid bodies and find induced currents from a rotating magnetic field of a PM via Faraday induction. The characteristic scales are set to $L = r_m$, $T = 1/\omega$, and $B = B_{rem}$. We begin with the expressions for $\mathbf{B}$ around a cylinder with transverse magnetization [17] put in a dimensionless form and added uniform angular frequency ω to the cylindrical magnet (Fig. 2a)

$$\mathbf{B} = \left(\frac{P_r}{\pi r}\cos(\varphi - t)\ ,\ \frac{P_\varphi}{\pi r}\sin(\varphi - t)\ ,\ \frac{P_z}{\pi}\cos(\varphi - t)\right), \tag{3}$$

where φ is the azimuthal angle and t is time. The functions $P_r,\ P_\varphi$, and P_z are related and contain elliptic integrals of first, second and third kind. In the slipless low-frequency approximation our $\mathbf{B}$ and $\mathbf{J}$ can be described by Maxwell's equations in potential formulation and Ohm's law [64]. The eq. for current density, $\mathbf{J}$, in a dimensionless form is

$$\mathbf{J} = -\nabla\phi - \frac{\partial \mathbf{A}}{\partial t} + \mathbf{v}\times\mathbf{B}, \tag{4}$$

where ϕ is the electric scalar potential and $\mathbf{A}$ is magnetic vector potential. For now we restrict ourselves to only stationary conducting solid with $\mathbf{v} = 0$ and leave further theory development with velocity considerations for later. Two components is enough for an arbitrary $\mathbf{A}$ that satisfies $\nabla\times\mathbf{A} = \mathbf{B}$ so for the sake of simplicity we set $A_\varphi = 0$ and perform integration

$$\mathbf{A} = \left(-\int rB_z d\varphi\ ,\ 0\ ,\ \int rB_r d\varphi\right) = \frac{\sin(\varphi - t)}{\pi}(-rP_z, 0, P_r). \tag{5}$$

Demanding charge conservation $\nabla\cdot\mathbf{J} = 0$ in the conducting body we find

$$\nabla^2\phi = -\nabla\cdot\frac{\partial\mathbf{A}}{\partial t} = -\frac{2P_z}{\pi}\cos(\varphi - t). \tag{6}$$

Thus, for electric potential we assume the form

$$\phi = -\frac{(f+h)}{\pi}\cos(\varphi - t), \tag{7}$$

where f is the particular solution and h is the complementary solution.

Particular solution is sought by setting $h = 0$ and looking for solution to eq.

$$\frac{\partial^2 f}{\partial r^2} + \frac{1}{r}\frac{\partial f}{\partial r} - \frac{f}{r^2} + \frac{\partial^2 f}{\partial z^2} = 2P_z. \tag{8}$$

Using relationships between functions $P_r,\ P_\varphi$, and P_z solution can be found to be

$$f = r^2 \frac{\partial(\frac{1}{r}\int P_\varphi dz)}{\partial r} = r\frac{\partial(rP_f)}{\partial r} \tag{9}$$

where $\int P_\varphi dz$ is integrated analytically and the solution is defined in terms of the new function P_f that contains elliptic integrals. The current density boundary conditions are enforced through the complementary solution h as

$$\left(\frac{\partial h}{\partial r} + P_f\right)\bigg|_{r=r_1,\ r=r_2} = 0, \qquad \frac{\partial h}{\partial z}\bigg|_{z=z_1,\ z=z_2} = 0. \tag{10}$$

The complementary solution is sought by performing variable separation and expanding z dependence of h in Fourier series. In doing so we have equation

$$\frac{\partial^2 h}{\partial r^2} + \frac{1}{r}\frac{\partial h}{\partial r} - \frac{h}{r^2} - a_n^2 h = 0, \qquad h = h_{00} + \sum_{n=0}^{N} h_n. \tag{11}$$

The solution for general case with arbitrary z_1 and z_2 is

$$\begin{cases} h_{00} = (C_{00} + C_{10})\,r + \dfrac{(C_{01} + C_{11})}{r} \\ h_n = (C_{In} I_1(a_n r) + C_{Kn} K_1(a_n r))\cos(a_n(z - z_1)),\ a_n = \dfrac{(n+1)\pi}{z_2 - z_1}, \end{cases} \tag{12}$$

where I_1 and K_1 are the modified Bessel's functions of first and second kind, respectively and C_{00}, C_{10}, C_{01}, C_{11}, C_{Kn}, and C_{In} are r_1 and r_2 dependent constants.

1.2. Scope and validation of the model

The time averaged volume force in the conducting body is only in the azimuthal direction and is equal to $\langle \mathbf{F} \rangle = F_\varphi \mathbf{e}_\varphi$, where $\mathbf{e}_\varphi$ is the azimuthal unit vector. The plot of the azimuthal time averaged volume force F_φ over cross section of ring (Fig. 3b) shows the force being mostly located in a boundary layer closer to the magnet. For result comparison over different parameters and geometries it is convenient to use the integral torque on a conducting body $M = \int_V rF_\varphi dV$.

The analytical current density and integral torque calculation was implemented using *Wolfram Mathematica* software and comparing with numerical solution gives good agreement in the linear region of the problem. Using simple experimental setup shown in Fig. 3a integral torque was measured experimentally with cylindrical and ring-shaped aluminium alloy conductors. The experimental setup was designed to allow for simple measurement of the force. A constant lever arm of length $47mm$ was provided by a disk connected through support rod to the conducting ring or cylinder. Numerically the problem was solved including induced magnetic field computation in three-dimensional (3D) geometry using software *COMSOL* for the experiment geometries with cylinder and ring conductors.

In Fig. 3c analytical integral torque is compared with numerical and experimental results of axially displaced cylinder by h_{cyl} or ring by h_{ring}. The transparent sectors depict three times the standard deviation for the experimental torque–frequency slope coefficient. Analytical solutions were scaled in such a way that one of the measurements are identical to the corresponding solution. It was done because aluminium alloy conductivity was not known. The counterweight measurement with $h_{ring} = 0$ mm for ring geometry was set to be the reference measurement. Our solution is valid for the magnet placed on axis of a full or hollow conducting cylinder (ring) and is of most importance where the geometric part of the magnetic field is significant and neither magnetic dipole nor infinite cylinder magnetic field approximations give appreciable results. Self-induction is not accounted for in our solution; however, we find that solution is accurate to high precision up to dimensionless frequencies ≈ 2 and with integral torque error $10 - 15\%$ up to dimensionless frequencies ≈ 3.

Although the presented analytical solution is true only for low rotational frequencies, our experiment example (Fig. 3c) shows that frequencies are high enough (15 rev/s) to be considered in real applications, such as molten metal stirring and mixing. In such application, however, we have to take flow velocity into account. In the first approximation, accounting for slip velocity can be done with eq. (2). Additionally, the obtained exact analytical magnetic field and current density expressions can be advantageous over numerical simulations when making parametric calculations.

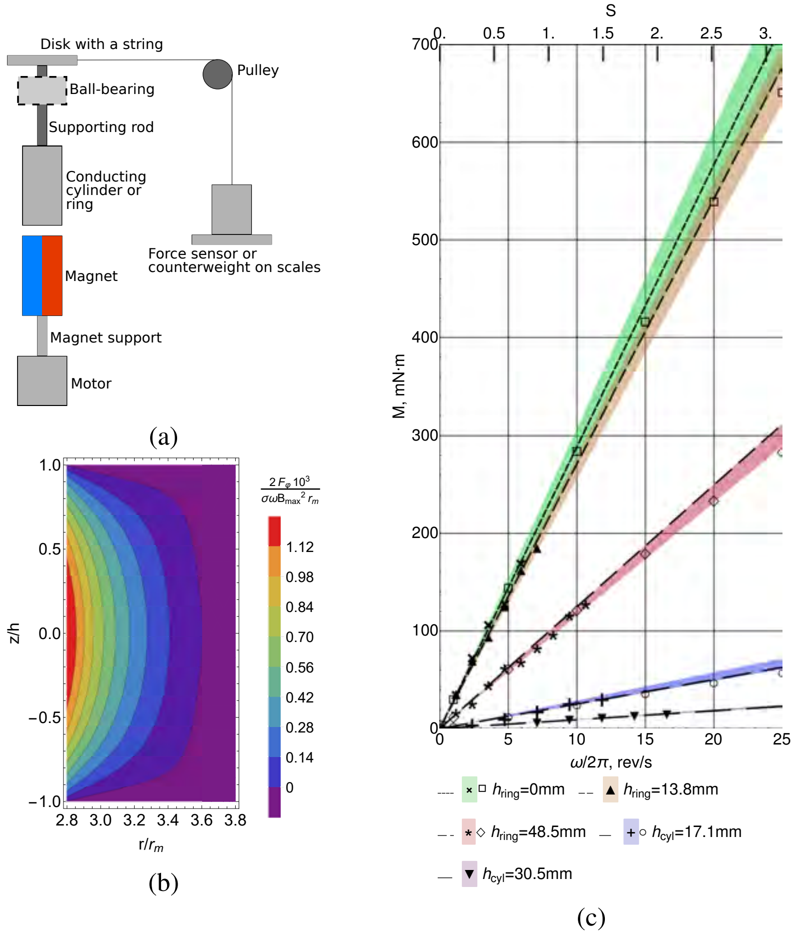

Figure 3. Sketch of the experimental setup (a). Analytical time-averaged azimuthal volume force in ring cross section (b). Comparison between analytical solution, *COMSOL* calculation and experimental measurements with counterweight, represented by dashed lines, empty symbols, and filled symbols, respectively (c).

2. RPM generated flow in cylindrical containers

In this section an RPM system – end field of rotating magnetic dipole – is considered for generating liquid metal flow in coaxial disc container. The setup is analyzed analytically and numerically with the emphasis on comparison with the corresponding experimental setup. The RPM system generates a similar type of flow as traditional RMF stirrers, but is suitable for cases with a large nonmagnetic gap or distance between magnet and metal. Traditional RMF stirrers generate an almost uniform magnetic field with a strong component perpendicular to the axis of rotation. However, when the liquid metal container is shallow, body force is more effectively generated with the axial component of the magnetic field. Such preference for the primary magnetic field direction can be seen in the design of PM pumps [6]. The nonmagnetic gap is maintained quite high in the considered setup to represent a possible design of an industrial device, where the temperature of molten metals is well above the ambient temperature and the container is covered with a heat-reflective material to avoid heat loss and damage to the surrounding environment. In such case, a dipole magnet system is the optimal magnetic field source [65, 10]. Many aspects of the RPM-induced flow have not been studied yet because it is a relatively new concept. On the other hand, the theory of RMF-induced flows is well established and can serve as the bases for our study of RPM-induced flow.

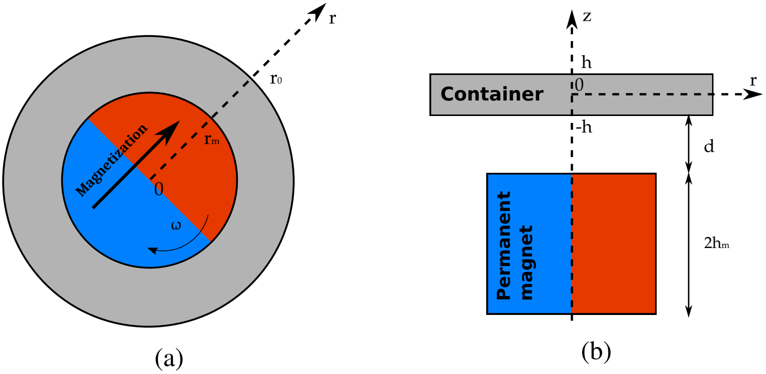

Figure 4. Sketch of the model: (a) bottom view of the model; (b) vertical cross-section through the cylinder axis.

The cylindrical container for the experimental setup was manufactured from an acrylic glass and was filled with room-temperature liquid GaInSn alloy. The magnet, which in the experiment was driven by an electric motor, placement coaxially at a distance d below the cylindrical container is illustrated in the sketch of our model system (Fig. 4). To maximize the axial component of magnetic flux density in the container and increase the stirrer efficiency, iron yoke sectors with height l and thickness w were placed on the poles of the PM without completely covering the magnet vertically. Most of the analytical and numerical calculations correspond to the experimental setup they are compared with. Therefore, unless specified otherwise, the parameter values used in the figures and calculations of this section are those corresponding to the experimental setup presented in Table 2. However, initially magnet without iron yokes is considered. Using ultrasound Doppler velocimetry (UDV) the experimental setup allowed for azimuthal velocity measurements up to 3 m/s in seven different radial positions with high temporal resolution but poor spatial resolution along the height.

Quantity	*Symbol*	*Value*
Magnet half-height	h_m	0.05 m
Magnet radius	r_m	0.06 m
Yoke height	l	0.06 m
Yoke thickness	w	0.02 m
Remanent magnetization	B_{rem}	1.42 T
Magnet rotation frequency	ω	1.95..19.5 Hz
Distance between magnet and metal	d	0.038 m
Metal cylinder half-height	h	0.015 m
Metal cylinder radius	r_o	0.1 m
Electrical conductivity	σ	3.27×10^6 S/m
Viscosity	ν	3.35×10^{-7} m^2/s
Density	ρ	6400 kg/m^3

Table 2. Values of quantities used in the experimental setup.

The dimensionless parameters in this section are defined based on characteristic scales $L = h$, $T = h^2/\nu$, and $B = B_{max}$, where $B_{max} = \max(\mathbf{B})$ is the PM-generated maximum magnetic flux density in the container. The inequalities $S \leq 3$, $Re_m \ll 1$, and $N \ll 1$ are roughly fulfilled in the experimental setup but assumed to be true in the analytical and numerical modelling. The condition $Re/Re_\omega \ll 1$ is not fulfilled but initially assumed true for analytical considerations. The final analytical velocity is obtained by applying slip correction from eq. (2).

The effective time-averaged azimuthal force can be described with $F_\varphi = 0.5\rho\Omega_f^2 r f$, where f is r-dependent function. In case of $f = 1$, Lorentz force is proportional to r, which is approximately true when considering RMF stirrers with a transverse magnetic field in low frequency regimes and containers with aspect ratio ≈ 1 [1]. If the given force is axially uniform, then $\Omega_f = B(\sigma\omega/\rho)^{\frac{1}{2}}$. On the other hand, if the volume force has axial variation, then the z-dependence can be accounted for by determining the effective Ω_f by equating the actual integral torque to that of the assumed distribution,

$$\Omega_f = \sqrt{\frac{\int r(2\langle \mathbf{F} \rangle/\rho) \cdot \mathbf{e}_\varphi dV}{\int r^2 f dV}}. \tag{13}$$

2.1. Analytical description

2.1.1. Boundary layer

When angular velocity of liquid metal is generated in an axisymmetric container, an almost constant angular momentum throughout the container's height is maintained, even in the presence of considerable axial variation of the body force [1]. The process bears some similarities with the Taylor–Proudman theorem. A strong secondary flow is generated, which is responsible for equalizing azimuthal flow in the axial direction. With the traditional RMF-generated turbulent liquid metal flow, the angular momentum generated in the axisymmetric container depends only on the integral value of the time-averaged body force and can be described using an effective force that varies linearly with the radius [1].

In the presence of radially linear volume force ($f = 1$), the solution for the boundary layer has been previously found [1] with the model of flow between two infinite disks, formulated in the form of von Kármán similarity variables

$$\mathbf{u} = (\Omega r F_b,\, \Omega r G_b,\, \Omega h_b H_b), \qquad p = 0.5\rho\Omega^2 r^2 + \rho\Omega^2 h_b^2 P_b, \tag{14}$$

where the argument of the functions F_b, G_b, H_b, and P_b is z/h_b and Ω represent the angular velocity of the core flow. Here, the cylinder's half-height, h, is set as the characteristic length scale of the core flow and the boundary-layer length scale as the von Kármán boundary layer thickness, $h_b = (\nu/\Omega)^{\frac{1}{2}}$. The ratio between these length-scales is $\epsilon = (\nu/\Omega)^{\frac{1}{2}}/h$. Inserting the variables from eq. (14) in the steady state incompressible N–S equation

$$\mathbf{u} \cdot \nabla \mathbf{u} = -\nabla \left(\frac{p}{\rho}\right) + \nu \nabla^2 \mathbf{u} + \frac{\langle \mathbf{F} \rangle}{\rho} \tag{15}$$

leads to the boundary layer equations

$$\begin{cases} F_b^2 + H_b F_b' - G_b^2 + 1 = F_b'' \\ 2F_b G_b + H_b G_b' = G_b'' + \dfrac{1}{2}\dfrac{\Omega_f^2}{\Omega^2} \\ H_b' + 2F_b = 0. \end{cases} \tag{16}$$

The obtained eq. system (16) with the assumption of negligibly small ϵ, which leads to elimination of the forcing term $0.5\Omega_f^2/\Omega^2$, has previously been considered and solved [1]. Our goal, however, is to study the effect of volume force on the boundary layer flow, so we retain the forcing term in eq. system (16) and seek solutions with small positive and negative force values near the boundary. Then the boundary conditions are

$$z/h_b = 0 : F_b = G_b = H_b = 0; \quad z/h_b \to \infty : F_b = \frac{1}{4}\frac{\Omega_f^2}{\Omega^2},\ G_b = 1, \tag{17}$$

where the boundary condition $F_b(\infty) = 0.25\Omega_f^2/\Omega^2$ originates from the assumption that far away from the boundary (in the core region), the Coriolis force is responsible for compensating the induced body force. Eq. (16) was rewritten with the coordinate transform $z = -1.5\log(1 - z_b)$, $z_b \in [0 : 1]$ and solved as a boundary problem with *Wolfram Mathematica* function *NDSolve* setting the “*Shooting*” method.

2.1.2. Core flow

The developed analytical model of RMF-generated flow [1] in axisymmetric containers predicts the axially invariant azimuthal flow in the core region (outside of boundary layers). The model velocity components in the core region are related by the in-compressibility equation,

$$u_z = -\frac{z}{r}\frac{d(ru_r)}{dr}, \tag{18}$$

and force balance between the Coriolis and induced volume force terms,

$$u_r\Gamma'(r) = F_\varphi r/\rho, \tag{19}$$

where the definition of the specific angular momentum is $\Gamma = u_\varphi r$. Due to in-compressibility, the flow rate through the boundary layers can be evaluated as the flow rate in opposite direction through the core region, $q = -\int_0^{r_0} 2\pi r u_z \mathrm{d}r$, where the integration goes until the boundary layer but the boundary layer is assumed very small compared to r_0. Furthermore, applying in-compressibility eq. (18), q can be expressed through u_r. Finally, using the force balance equation in the core (19), it is possible to relate the boundary layer flow rate to the induced volume force. Integral boundary layer flow transport equation in such formulation has been solved previously [1] and the resulting expression for specific angular momentum was found to be

$$\Gamma_c = (2 \cdot 0.0372)^{-\frac{5}{9}}\,\chi_1^{-\frac{1}{9}}\left(\frac{r_o^3}{r^3}\mathcal{U}\right)^{\frac{5}{9}} h^{\frac{1}{2}}\Omega_f r^{\frac{3}{2}}\left(\frac{h\Omega_f (r^3/r_o)^{\frac{1}{2}}}{\nu}\right)^{\frac{1}{9}}. \tag{20}$$

The function $\mathcal{U}$ was sought as a solution to differential equation

$$\mathcal{V}''(\mathcal{G} - \mathcal{V}) = 2\chi_1\mathcal{G}'\mathcal{V}', \tag{21}$$

where

$$\mathcal{V}(\eta) = \int_0^\eta \mathcal{U}(\eta) d\eta, \qquad \mathcal{G}(\eta) = \int_0^\eta \eta^3 f(\eta) d\eta, \qquad \eta = r/r_o. \tag{22}$$

Eqs. (21) and (22) were originally solved with a volume force that is proportional to r, meaning $f = 1$ [1]. We have complemented the eq. (22) with our introduced force function f and found the solution to (21) for three forcing functions

$$\begin{aligned} &f_1 = \eta^a, \\ &f_2 = 1 - \eta, \text{ and} \\ &f_3 = 1 - b\eta^2 + (b-1)\eta^3 \end{aligned} \tag{23}$$

to be

$$\begin{aligned} &\mathcal{U}_1 = \left(1 - \frac{2(a+4)}{(a+3)}\chi_1\right)\eta^{(a+3)}; \qquad \chi_1 = \frac{(a+3)}{2((a+4) + r_o/h)}, \\ &\mathcal{U}_2 = -\frac{1}{3}\eta^3 + \frac{1}{4}\eta^4, \text{ and} \\ &\mathcal{U}_3 = -\frac{1}{3}\eta^3 + \frac{b}{5}\eta^5 - \frac{(b-1)}{6}\eta^6, \end{aligned} \tag{24}$$

respectively. For solutions $\mathcal{U}_2$ and $\mathcal{U}_3$ is found to satisfy the eq. (21) with the parameter value $\chi_1 = 0.5$. Function f_1 is a more general description of RMF induced force distribution and inserting parameter value $a = 0$ in the corresponding solution $\mathcal{U}_1$, recovers the original solution obtained in [1]. The force functions f_2 and f_3 describe RPM induced force distribution. The corresponding solutions of $\mathcal{U}$, however, are negative and simply inserting them in eq. (20) would result in a complex value. To avoid this, we take the absolute value of the expression presented in eq. (20), $\Gamma = |\Gamma_c|$.

2.2. Numerical methods

The hydrodynamics and electrodynamics numerical calculations were performed with open-source code *OpenFOAM* and *Elmer*, respectively. The communication between the programs were provided by the open-source code *EOF-Library* [63]. A solution to the steady-state incompressible N–S equation (15) in a closed container was sought with the Semi-Implicit Method for Pressure Linked Equations algorithm. A one-equation turbulence model, Spallart–Almaras [66], was used because it required the least calculation time to reproduce the numerical results of a previous study [1], compared with multiple other RANS models (k-ϵ, k-ω, and k-ωSST) and, thus, allowed to conduct a wider parametric study of the system.

A structured 3D mesh was used for hydrodynamic calculations and comprised of ≈ 1.7 million elements. Overall, the 3D mesh for EM calculations comprised of $\approx$ 160 thousand elements without yokes and $\approx$ 280 thousand elements with yokes. An *Elmer* harmonic solver with time dependence $\exp(i\omega t)$, where i is the imaginary unit, was used to calculate the time-averaged force. $\mathbf{M} = (\mathbf{e}_x - i\mathbf{e}_y)B_{rem}/\mu_0$ is our definition of the complex magnetization. The real part of the magnetization represents the rotation angle when magnet poles are aligned with the x-direction and the imaginary part represents the position when magnet poles are aligned with the y-direction.

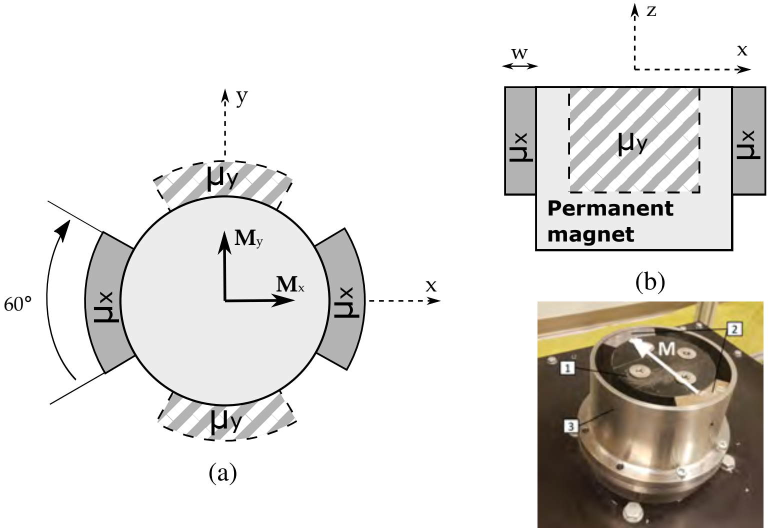

(a)

(b)

(c)

Figure 5. Yoke domains in harmonic solver: (a) top view; (b) side view. Experimental magnet with yokes: 1 – permanent magnet, 2 – ferromagnetic yokes, 3 – stainless steel rim (c).

With harmonic solver the magnetic vector potential and electric potential is found by solving the equation system

$$\begin{cases} \mathbf{J}_k = -i\omega\sigma\mathbf{A}_k - \sigma\nabla\phi + \sigma\mathbf{u}\times(\nabla\times\mathbf{A}_k) \\ \nabla\times\left(\dfrac{1}{\mu}\nabla\times\mathbf{A}_k\right) = \mathbf{J}_k + \nabla\times\mathbf{M}_k, \end{cases} \tag{25}$$

where indices $k = 1,\ 2$ have been introduced to represent variables of two separate equation systems. Then, $\mathbf{B}$ can be calculated by taking curl of the magnetic vector potential.

In the experimental setup, ferromagnetic yokes are introduced on the poles of the magnet (Fig. 5c), which increases the effective magnet radius, and consequently, the induced volume force. The yokes are placed in a manner that they do not completely cover the magnet vertically (Fig. 5b), increasing vertical magnetic flux density in the direction of liquid metal container. The permeability of the yokes in each quarter period of rotation (Fig. 5a) should be correctly represented in the harmonic solver. To account for this numerically, the harmonic solver was modified as follows. In the first eq. system ($k = 1$), we solve only for the contribution of the x-direction component of the magnetization vector, which is the real part of $\mathbf{M}$. Thus, we have

$$\mathbf{M}_1 = M_x \mathbf{e}_x = \mathbf{e}_x B_{rem}/\mu_0 = \mathcal{R}e(\mathbf{M}),\ \mu_x = \mu_{ferro},\ \mu_y = \mu_0, \tag{26}$$

where yoke in the x-direction is ferromagnetic, whereas yoke in the y-direction is non-magnetic (domain acts as vacuum). Similarly, in the second eq. system ($k = 2$), we only solve for the contribution of the y-direction component of the magnetization vector in which case only imaginary part of $\mathbf{M}$ is left. We get

$$\mathbf{M}_2 = M_y \mathbf{e}_y = -i\mathbf{e}_y B_{rem}/\mu_0 = i\mathcal{I}m(\mathbf{M}),\ \mu_x = \mu_0,\ \mu_y = \mu_{ferro}, \tag{27}$$

where now yoke in the y-direction is ferromagnetic, but yoke in the x-direction – non-magnetic. The permeability of the ferromagnetic yoke, μ_{ferro}, is calculated from an iron H–B curve. The final vector potential and scalar potential are the sum of both eq. system results

$$A = A_1 + A_2, \qquad \phi = \phi_1 + \phi_2. \tag{28}$$

2.3. Results and discussion

Fig. 6a shows the axial distribution of scaled azimuthal and axial velocities and the components of force balance equation. The viscous term becomes important in the force balance equation closer to the center of the cylinder. For example, at $r/r_o = 0.2$, the Coriolis term, together with the viscous term compensates the forcing term away from the boundaries at $z/h \in [-0.7, 0.7]$. The numerical calculations of RPM bottom-stirred flow (Fig. 6a) show a rather counter-intuitive result – the maximum velocity is observed on the opposite side of the RPM, which generates the flow. However, the explanation is given by the asymptotic boundary layer solutions, which qualitatively agree with numerical results. Fig. 6b shows that the presence of an accelerating (positive) body force near the vertical boundaries decreases the peak value of azimuthal velocity. In contrast, the presence of a decelerating (negative) body force increases the peak azimuthal velocity.

The integral torque for various container aspect ratios were compared and indicate that stirring from bottom becomes more effective as the container height decreases. However, the container aspect ratio also affects the flow radial distribution. The force radial distribution has no effect on the azimuthal velocity

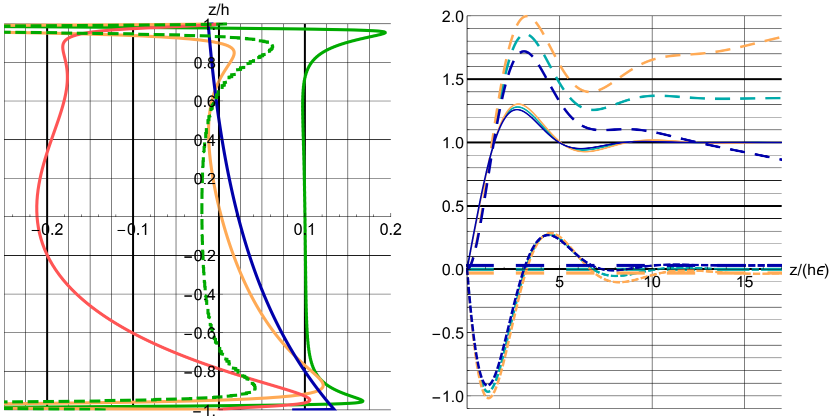

(a) (b)

Figure 6. Distribution of flow characterizing quantities: (a) axial distribution of $\Gamma' u_r/(\Omega r)^2$, $(\nu+\nu_t)\nabla^2 u_\varphi/(\Omega^2 r)$, $F_\varphi/(\Omega^2 \rho r)$, $u_z/(10\Omega h\epsilon)$, and $u_\varphi/(\Omega r)-0.9$ plotted with light orange, green dashed, dark blue, light red, and dark green lines, respectively, at $r/r_o = 0.2$ with $d = 0.15$ and $h = 0.03$; (b) asymptotic boundary layer solutions for G_b, H_b, $2F_b$, and force term, represented as solid, short-dashed, dotted and long-dashed lines, respectively, with force terms $0.5\Omega_f^2/\Omega^2 = -0.03$ (light orange), 0 (cyan), and 0.03 (dark blue).

radial distribution, as long as the RPM bottom-stirred container height–diameter aspect ratio ≈ 1. In such case, the resulting azimuthal velocity distribution can be explained by the existing theory of RMF-induced flows, which assumes radially linear force distribution [1]. On the other hand, when shallow containers with height–diameter aspect ratio $\ll 1$ are considered, the numerically calculated and experimentally measured azimuthal velocity show that the force radial distribution affects the velocity distribution.

Fig. 7a shows the axially-averaged analytical solution of time-averaged torque distribution radially with graphs fitted for various f functions, where Ω_f is calculated according to eq. (13). The RMF-induced force distribution is fitted with forcing function f_1 and parameter $a = 8.64$, whereas the RPM-induced force distribution is fitted with f_2 and f_3, where parameter $b = 2.63$ is used. In the example with container aspect ratio $h/r_o = 1$, the analytical description with $f = 1$ works rather well, whereas in the example of our experimental setup, where the height-diameter ratio is small $h/r_o = 0.15$, the force radial distribution becomes important and the analytical description with functions f_2 and f_3 fits the azimuthal velocity profile much better (Fig. 7b).

In our our RPM stirrer setup (Fig. 4) $r_m/r_o = 0.6$, which leads to the induced torque maximum at around $r/r_o = 0.6$ (Fig. 7a). Furthermore, the resulting azimuthal velocity maximum is also near $r/r_o = 0.6$ (Fig. 7b). This result is qualitatively different from the traditional RMF-induced flow, where the maximum velocity is near the radial walls of the container.

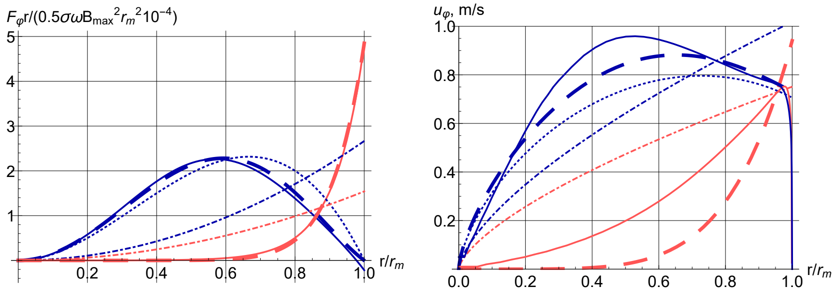

(a) (b)

Figure 7. Induced torque (a) and azimuthal velocity (b) radial distribution for a RPM (dark blue) and a uniform RMF (light red) stirrer – exact/numerical result, $f = 1$, $f = f_2$(for RPM) with solid, dashed–dotted, and dotted lines, respectively, and $f = f_1$(for RMF) and $f = f_3$(for RPM) with thick dashed lines.

The low-frequency analytical force solution was used to determine the effective parameters that correspond to the magnet system with yoke. It was found that in our case (Fig. 5) increasing the effective magnet radius by 12.5% to $r_m = 0.0675$ corresponds to the magnetic field and induced force of a magnet with yokes. The numerical calculations show that adding yokes increases the maximum volume force at the container bottom wall by 15.8% and the integral torque by 27.8%. Consequently, the RPM-generated maximum velocity in the container is increased by 6%–11%, thus increasing the stirrer efficiency.

The numerically calculated bottom-stirred flow in shallow cylinders (Fig. 7a) predict azimuthal velocity maximum at around $r = r_o/2$ with the peak value near the top boundary. The asymmetric meridional swirl is the result from the Coriolis force compensating the body force axial distribution, as follows from eq. (19). However, the meridional flow in the core is too small ($< 10\%$ of the azimuthal velocity) to disturb the azimuthal flow. This is not the case near the boundaries, where the maximum meridional velocity magnitude is $\approx 30\%$ of the maximum azimuthal velocity. However, here the nonlinearities can be described with the asymptotic boundary layer equations (16).

It was found that combining the analytical descriptions of a RPM-induced force with RMF-induced flow [1] a velocity radial profile is obtained that agrees quite well with the numerical and experimental data (Fig. 8b). As expected, a

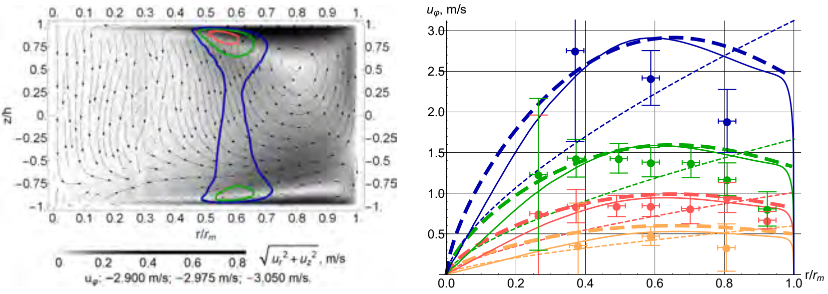

(a) (b)

Figure 8. Numerically calculated density and vector plot of meridional flow $\mathbf{v}$ and few contours of azimuthal velocity near the maximum value plotted in the vertical half-plane at magnetic rotation frequency 19.5 rev/s (a). Radial distribution of u_φ at $z = 0$ and magnetic rotation frequencies 1.95 rev/s (light orange), 3.9 rev/s (light red), 7.8 rev/s (dark green), and 19.5 rev/s (dark blue) for analytical $f = 1$, $f = f_3$, numerical and experimental plotted with dotted, dashed, thick solid lines, and filled circles, respectively (b).

better velocity profile agreement was obtained with the function f_3, which is a better fit for azimuthal force distribution in comparison to the function f_2. The experimental error bars in Fig. 8b depict three standard deviations from the mean of the collected UDV measurements for velocity. The error bars in the radial direction are due to the UDV probe beam thickness. Main features of the analytical and numerical velocity profiles agree with the experimental measurements – all results indicate negative slope toward the radial boundary, suggesting that the velocity maximum is closer to the center of the cylinder located at around $r = r_o/2$. Thus, a qualitative difference between a velocity profile in a cylinder with aspect ratio ≈ 1 is demonstrated.

3. Flow instability and bistability in a ring shaped container

In this section an RPM generated flow in a surrounding ring-shaped container is considered (Fig. 9). This configuration was chosen because of its effective use of a PM due to its magnetic field lines mainly closing through the metal in all directions. This configuration also corresponds to a centrifugal pump [11, 7] but, depending on geometric parameters, can also act as an effective stirrer. We set the characteristic scales to $L = h$, $T = h^2/\nu$, and $B = B_{max}$. For simplicity, the inner radius and half-height of the ring were set equal to each other ($r_i = h$).

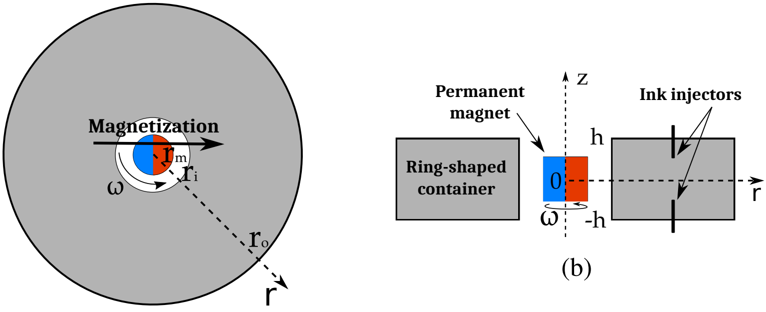

(a)

(b)

Figure 9. Sketch of the model: (a) top view of the model and (b) a vertical cross-section through the cylinder axis

We require $Re/Re_\omega \ll 1$, $Ha \ll 1$, and $S \ll 1$. It follows that $Re_m \ll 1$ and $N \ll 1$ are fulfilled as well. With these assumptions the EM force does not depend on the liquid velocity but simply serves the purpose of flow generation. As a result, the time-averaged volume force is axially symmetric with its only nonzero component in the azimuthal direction, which can be expressed in a dimensionless form as $Ta\ f(r, z) = (h^3/\nu^2\rho)F_\varphi$, where the definition of Taylor number is $Ta = 0.5Ha^2Re_\omega$. The dimensionless N–S equation then takes the form

$$\frac{\partial \mathbf{v}}{\partial t} + \mathbf{v} \cdot \nabla \mathbf{v} = -\nabla \tilde{p} + \nabla^2 \mathbf{v} + Taf(r, z)\mathbf{e}_\varphi, \qquad (29)$$

where $\tilde{p} = p/P$ is the dimensionless pressure. For additional simplicity, the magnet half-height and radius are set equal to each other ($h_m = r_m$). The RPM-generated volume force distribution, $f(r, z)$, has a pronounced maximum at $z = 0$ and $r = r_i$, which is essential for the development of the radial jet [67]. Using the analytical volume force solution, it was established that a finite-size magnet is well approximated by a dipole when $r_o/h = 0.54$, as in the experimental setup (Fig. 10).

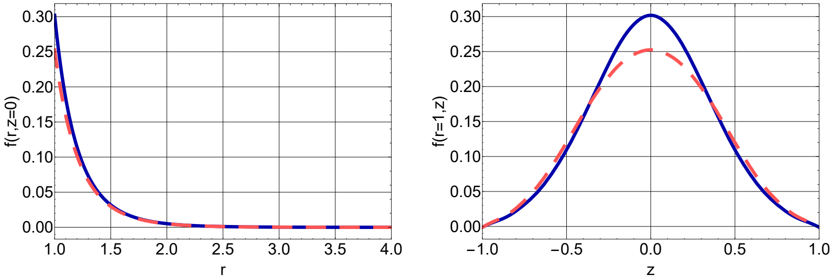

(a) (b)

Figure 10. Magnetic dipole (dark blue solid lines) and finite size magnet with $r_o/h = 0.54$ (red dashed lines) induced volume force spatial distribution: (a) radially at $z = 0$; (b) axially at $r = 1$.

3.1. Numerical methods

The solution to eq. (29) was found by performing DNSs with two independent numerical methods: the open-source software OpenFOAM and spectral methods. OpenFOAM mesh was generated with Gmsh software and consisted of structured hexahedrons. Calculations were performed with $(0.9..7.2) \times 10^5$ elements depending on geometry and Ta. Result saving interval was 0.005 in viscous time. Alternatively, the 3D spectral simulation program was used with $(0.7..1.8) \times 10^5$ points of spatial resolution and result saving interval varied from 0.0025 to 0.015 depending on Ta.

During the initial study it was found that larger aspect ratio of the ring, $R = r_o/r_i$, leads to lower critical Re. Furthermore, for $R > 3.2$ and sufficiently large Ta two mutually symmetric steady solutions emerge. To reduce the number of parameters and be well in the regime where the symmetric states manifest, further study was limited to one ring aspect ratio, namely $R = 4$. Additionally, the flow dependency on Ta was investigated.

The direction of the meridional flow – clockwise or anticlockwise – represent the two dominating attractors of the system. The system is symmetric with respect to the axial midplane, so $\mathbf{v}_z(r, \varphi, z = 0)$ plotted against the Taylor number was chosen for constructing bifurcation diagram. A hysteresis loop was found by calculating the decrement of the system. The leading eigenmode of the system, $\lambda_r + i\lambda_i$, was evaluated by fitting the computed velocity time dependency at a monitoring point with the function $f_{inst}(t) = A + B\sin(\lambda_i t + \varphi)\exp(\lambda_r t)$.

When a cyclic solution was reached, the Ta was decreased in small steps until the cyclic solution returned to a steady-state solution.

At larger Ta values, the flow enters an on–off intermittent regime, where due to short intermittent bursting of system variables the system can transition between the attractors, after some random time. When the system is in the chaotic switching regime, the fluctuation size is comparable to the size of the signal; thus, data over long time series is necessary to distinguish states with reasonable confidence. To distinguish the system attractors, first, time series signal from the probes at $(r, z) = (2.5, \pm 0.5)$ were subtracted from each other to reduce noise. Denoting the obtained signal s_0, it was then normalized according to

$$s_1 = (s_0 - \langle s_0 \rangle)/(2\langle |s_0| \rangle) + 0.5, \tag{30}$$

where s_1 is the normalized signal. As a result, signal value 0 corresponds to one attractor, whereas value 1 to the other attractor. For the final step, a threshold, Δ_{th}, is chosen and time steps are sorted according to

$$s_2(t) = \begin{cases} 0, & s_1(t) < 0.5 - \Delta_{th} \\ s_1(t - \Delta t), & 0.5 - \Delta_{th} \leq s_1(t) \leq 0.5 + \Delta_{th} \\ 1, & s_1(t) > 0.5 + \Delta_{th}. \end{cases} \tag{31}$$

The sorting from probe signal could be interpreted as the zeroth iteration. To improve the results, an integral measure – the kinetic energy of velocity fluctuations with respect to each of the system states integrated over the entire domain – was obtained according to $e_i = 0.5(\mathbf{v}_i - \mathbf{v}) \cdot (\mathbf{v}_i - \mathbf{v})$, where $i = 1, 2$ corresponds to the time-averaged velocity of each state. The whole procedure was iteratively repeated and it was found that the relative difference after one or two iterations is less than 1%. Thus, the sorted velocity angle signal from probes should already represent the system regime. Another integral measure – the mean azimuthal vorticity in the container,

$$\Omega_\varphi = \frac{1}{V} \int_V (\nabla \times \mathbf{v}) e_\varphi \mathrm{dV}, \tag{32}$$

should also be a good indicator of which attractor the system is in.

To investigate the statistical nature of the system, τ, the time intervals between transitions of the sorted signal from eq. (31), were collected. Next, the transition length step, $\Delta\tau$, was chosen as a multiple of the smallest obtained transition interval, $\Delta\tau = k \min(\tau)$, where k is the multiplication factor. Finally, the number of transition occurrences, $N(\tau)$, were calculated in an interval $\tau \in (n\Delta\tau, (n+1)\Delta\tau]$, where $n = 0, 1..n_{max}$ and $n_{max} = \mathrm{ceiling}(\max(\tau)/\Delta\tau)$.

3.2. Experimental methods

The basic concept for observing flow direction experimentally is to use a transparent electrolyte and introduce a contrasting solution through probes.

Hydrochloric acid has good conductivity at moderate concentrations compared to other acids [68] and even more so compared to salt solutions. A compromise between safety (10.4% w.w) and electrical conductivity ($\sigma = 71$ S/m) [68] was chosen to be a concentration of 3-mol/dm^3 HCl solution.

Finding a reliable method for probing the flow direction was more difficult. Initially silk threads attached to inner wall were considered. However, they tend to tangle up and turned out to have too much inertia to be useful in such slow flow regimes. Another option was to introduce ink to the liquid. A candidate compound was potassium permanganate because it reacts with HCl forming transparent solution. However, the reaction also produces bubbles that cover the top wall of the container that quickly obstructs the view. Additionally, after several hours the solution saturates and turns dark brown making it even more difficult to see the flow direction. Alternatively, pH indicator Bromphenol blue was considered for probing the flow. Its colour changes from dark blue to light yellow when pH of the solution changes basic to acidic. However, indicator usage is limited to close proximity of the probe because the colour change happens too quickly to develop ink “tail” that can be recognized in a photograph. Additionally, solution saturated after several hours which limited the length of the experiment.

Few additional problems surfaced during initial experiments. One of which is that although medical needles are made from stainless steel, they will react with strong acid, which in turn will change the specified probe locations, produce bubbles, and darken the solution with the inherent dark brown colour of iron(III) chloride. Another problem was due to the use of pressure driven flow for probes. One medical enteral feeding bag was used for multiple probes which lead to some probes not working due to different pressure resistances. Additionally, providing pressure with height difference lead to decreasing pressure during the experiment. As a result, probes with larger pressure resistance stopped working.

Another concern was the density of the probe compound in comparison with the density of the solution in the container, which could lead to buoyancy driven flow and disturb the main flow. In the initial experiments the density of HCl solution was decreased by adding alcohol mixture (65% ethanol and 35% isopropyl alcohol). However, testing multiple combinations of solution was difficult due to volatility of alcohol. Additionally, the physical properties of resulting solution could not be found in the literature.

To avoid problems listed above, multiple improvements were made to the experimental setup. The solution in the container was composed of the same components that entered the container from the probes. Additionally, coloring ingredient was chosen such that it would not react with HCl. It ensured that the solution in the container maintained the same composition throughout the experiment. Solutions from two of the probes were colored with $CuCl_2$ but the other six probes with $ZnCl_2$. $CuCl_2$ and $ZnCl_2$ salts have similar density,

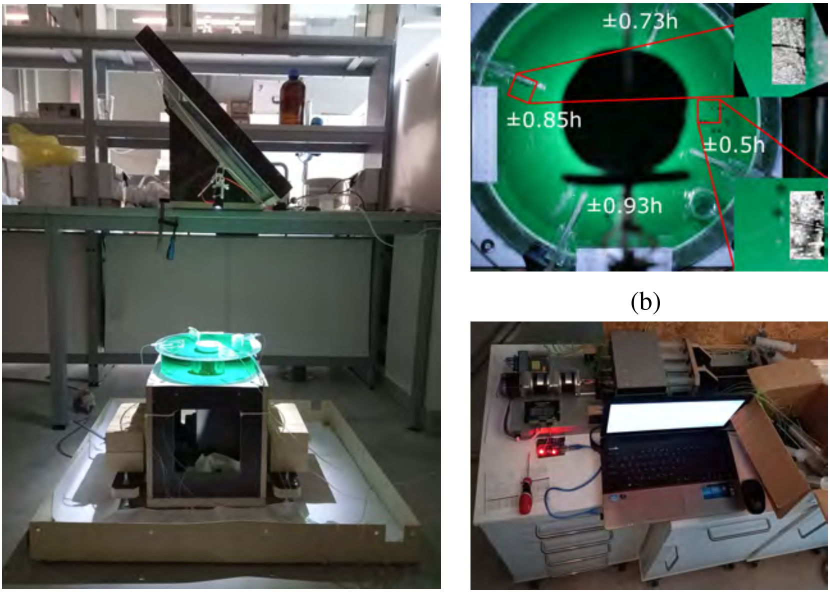

(b)

(a)

(c)

Figure 11. Experimental setup: (a) side view; (b) mirrored top view and zoomed-in view of the dye flow; (c) pump and its control system.

which facilitated the equalization of solution densities. The solution with $CuCl_2$ is green and was intended to work as ink, whereas solution with $ZnCl_2$ is transparent and served the purpose of diluting the color of the final solution in the container. The choice for $CuCl_2$ concentration of c_{CuCl2} =1.5 mol/dm^3 was based on the observed color intensity of the solution, which, when prepared in large containers, appeared to be sufficiently dark to serve the purpose of ink. However, in the experimental setup, where the solution is introduced in small quantities, $CuCl_2$ solution color intensity was not sufficient to distinguish it from the solution in the bulk of container. This problem was solved by using a point-like light-emitting diode, which produced sharp shadows of jets from the probes. The shadows were used to indicate the flow direction, which enabled not just the two probes with $CuCl_2$ solution, but all of the probes to be used for flow observation.

For the chosen $CuCl_2$ and HCl solution at 25°C the calculated density and viscosity is $\rho = 1215$ kg/m^3 and $\nu = 1.333 \times 10^{-6}$ m^2/s, respectively [69]. Experimentally it found that c_{ZnCl2} =1.89 mol/dm^3 of $ZnCl_2$ is required to equalized the densities between mixtures and avoid buoyancy effects. Based on a crude estimate, electrical conductivity for our setup with concentrated solutions of $CuCl_2$ and $ZnCl_2$ in mixture with HCl was found to correspond to 4-mol/dm^3 HCl solution, $\sigma = 80$ S/m.

The solution was introduced in the container through heat-shrink tubes, which were placed at various heights: z=± 0.5h, ± 0.73h, ± 0.85h, and ± 0.93h, where $h = 0.037$ m and the axially opposite probes were placed 22.5° apart to be distinguishable from each another (Fig. 11b). Each pair was separated by 90°and positioned at radial position $r = (r_i + r_o)/2$. A custom-made pump was constructed to simultaneously move eight syringes, each dedicated to a separate probe (Fig. 11c). The syringes were placed on a linear actuator moving at 1 μm/s, which provided reliable flow of 1.95 mm/s velocity for the solution entering the container from probes.

A mirror was placed above the experiment at 45°, which enabled to view the top of the container from side at a safe distance. Placed 5 m away from the mirror, a digital camera recorded the top view of the container with time-lapse photography (Fig. 11a). The experiment was conducted using two consecutive time-lapse recordings, where the time interval between pictures was set to 4 s and each of the recordings lasted for 11 h, 6 min, and 36 s.

The recorded pictures were stabilized with software Blender (available at https://www.blender.org/). Only those areas near the probes were kept. Additionally, the images were converted to gray scale and their contrast was increased. The ImageJ Ridge detection plugin [70, 71] was applied to the processed images and the coordinates of detected curves were extracted. The direction of the flow was obtained by approximating each curve with a slope and finding the slope coefficient.

3.3. Results and discussion

3.3.1. Numerical results

First, the relationship between the critical Re and the aspect ratio of the ring ($R = r_o/r_i$) was found. Namely, larger aspect ratio leads to lower critical Re (Fig. 12d). Thin-ring flow when $R < 2$ resembles a uniform RMF generated well-known flow with almost solid body rotation in the core (Fig. 12a). However, in the wide ring configuration when $R > 3$, a pronounced outward radial jet develops at the midplane, which decreases flow stability and the liquid is more stirred than pumped. A possible explanation for the development of the radial jet could be that the Taylor–Proudman theorem does not hold in the viscous boundary layer at r_i, where the volume force is concentrated. On the other hand, when R is small the geometry enforces sufficiently strong secondary circulation to maintain the mechanism for angular momentum vertical transport. More insight may be gained by comparing the terms of force balance equation for azimuthal direction (Fig. 13). When $R = 1.5$, volume force is mainly compensated by Coriolis force and boundary layers develop near vertical boundaries (Fig. 13b), similarly as it does for the flow in cylinders. In contrast, the volume force is a smaller order term in the wider ring configuration (Fig. 13a). In the latter case, Coriolis and convective force are the leading terms in the force balance equation.

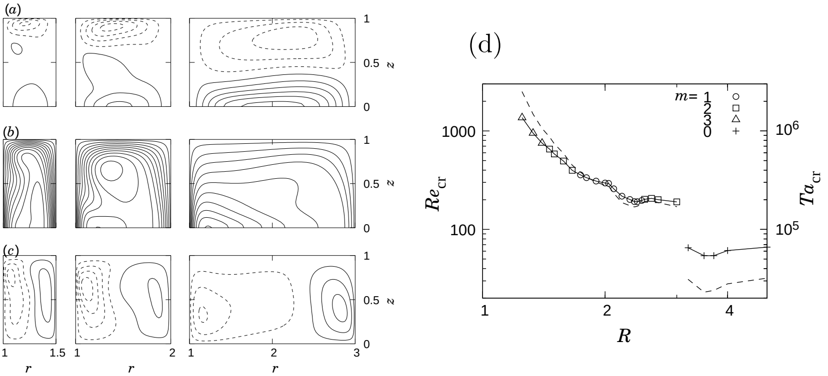

Figure 12. Isolines of radial (a), azimuthal (b), and axial (c) velocity in near-critical flow for $R = 1.5$, 2, and 3 from left to right. The isoline step is 58.3, 29.6, and 19 for $R = 1.5$, 2, and 3, respectively, being 10% of the maximum velocity. Dashed lines display negative values. Critical Reynolds number, Re_{cr}, (solid lines) and critical force parameter, Ta_{cr}, (dashed lines) dependence on ring aspect ratio, where m is the azimuthal wave number of the least stable perturbation (d).

Next we explore the development of instability toward turbulence as the magnetic force is progressively increased in an even wider ring configuration. This geometry is characterized by a significant drop in the critical EM force parameter value and the change in the nature of the instability. For large ring aspect ratios ($R > 3.2$), the flow becomes considerably destabilized with the critical force parameter dropping by a factor of three (Fig. 12d).

At low Taylor number, a radial jet develops at the midplane and it is symmetric with respect to the height of the ring. When the Taylor number is increased to $Ta = 2.7 \times 10^4$, a pitchfork bifurcation occurs (Fig. 14a) and the radial jet turns upwards or downwards with equal probability.

Results from spectral methods and *OpenFOAM* calculations show good agreement. For example, *OpenFOAM* calculations show that subcritical periodic solutions emerge at $Ta = 5.8 \times 10^4$ with $\lambda_i^{cr} = 8.95$. Similar results were obtained with spectral methods, where the critical value of $Ta_{cr} = 5.485 \times 10^4$ with $\lambda_i^{cr} = 9.137$ (Fig. 14b). Furthermore, from *OpenFOAM* calculations the limit cycle persists down to $Ta = 4.5 \times 10^4$, whereas it drops back to the stationary solution at $Ta = 4.4 \times 10^4$. Similarly with spectral methods the

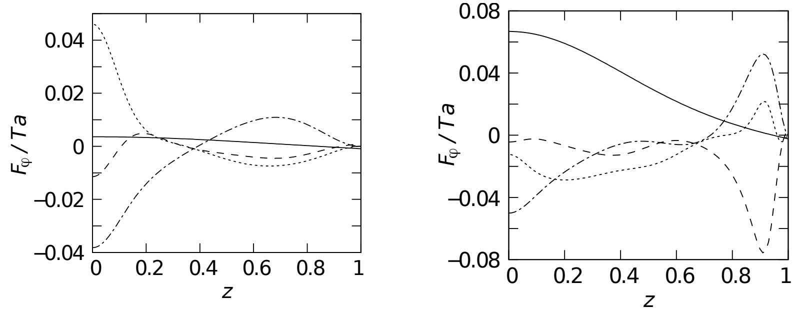

(a) (b)

Figure 13. The azimuthal force balance in the marginally stable base flow in vertical section $r = 2$ at $R = 3$, $Ta = 1.7 \times 10^5$ (a) and $r = 1.25$ at $R = 1.5$, $Ta = 7.4 \times 10^5$ (b). Convective, Coriolis, viscous, and magnetic terms of stationary v_φ solution are displayed by dotted, dashed—dotted, dashed, and solid lines, respectively. The sum of all curves is zero.

ensuing limit cycle solution could be followed down to $Ta = 4.4 \times 10^4$, whereas the flow fell back to the steady state at $Ta = 4.39 \times 10^4$ (Fig. 14b).

Tertiary instability developed at $Ta = 1.2 \times 10^5$ (Fig. 14a), but above $Ta = 2 \times 10^5$ the system enters a turbulent state around one of the mirror-symmetric branches where the fluctuation energy at times is large enough to trigger transition toward the other attractor (Fig. 15a). The energy difference between the two branches of our system significantly exceeds the typical fluctuation energy, resulting in prolonged switching intervals of the order of 100 viscous time units (Fig. 15a). Additionally, it is possible to observe very short or even failed transitions (Fig. 15a at $t = 25, 130, 210$). For larger Ta, the turbulent fluctuations increase, and transitions occur more often (Fig. 15b) until the energy of the fluctuations are of similar magnitude as the energy gap between the attractors (not shown).

In the regime of turbulent bistability, an appropriate approach is to average the flow around each state, as time-averaging over the whole duration of calculation may lead to skewed conclusions. A good indicators of the global flow state of the system are radial and axial flow probes. The probes can serve as an initial approximation, that can then be iteratively improved by sorting transient flow states according to their energy difference (Fig. 15b) in the current approximation. For the considered system, such sorting changed less than 1% after the first or second iteration. In the presence of noise a more comprehensive plot can be obtained by applying a moving average. A moving average of the probe signal is in good agreement compared to the signal s_2 from the sorted energy differences and the mean azimuthal vorticity calculated from eq. (32), as

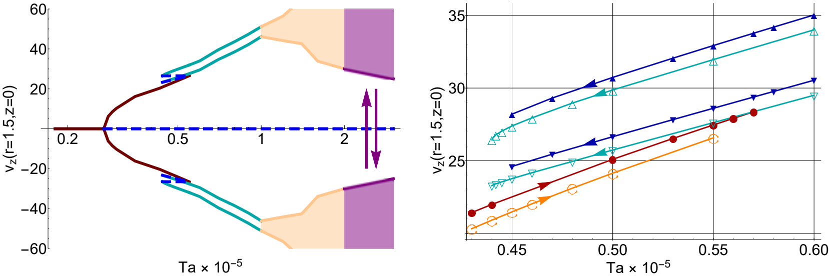

(a) (b)

Figure 14. Bifurcation diagram: (a) global view where the steady-state, cyclic, aperiodic, on–off intermittent and, implied repelling solutions are indicated with red, cyan, light orange, purple and, blue dashed lines, respectively; (b) *OpenFOAM* (filled symbols) and spectral method (empty symbols) result comparison near the hysteresis loop where the steady-state solutions, maximum values of cyclic solutions and, minimum values of cyclic solutions are plotted with circles, upward triangles, and downward triangles, respectively.

shown in Fig. 15b. Afterwards, the time-averaged flow and velocity fluctuations can be computed with respect to the separated states. The unsorted time-averaged v_r and velocity fluctuations (Fig. 16a,c) leads to different qualitative interpretation of the results compared to averaging with respect to the “up” and “down” attractors (Fig. 16b,d). The interpretation of Fig. 16a,c is that two small mirror-symmetric swirls with large fluctuations are present in the meridional plane, whereas Fig. 16b,d leads to the conclusion that the meridional plane is dominated by one large swirl that has smaller fluctuations but switches direction from time to time. The DNS approach may help to identify the multiple states of the system, however, DNS is expensive and not always feasible. The presented low Re example may help to develop and test alternative methods.

The statistical nature of the system can be revealed by collecting time intervals τ between regime changes and plotting their occurrence in a log–log plot. We have plotted $N(\tau)$ of our system alongside the switching intervals of geomagnetic reversals (GRs) [55] (Fig. 17a). Similar to GRs and for many other systems in nature $N(\tau)$ of our system also follows the $-3/2$ law.

The influence of external factors on the system was not examined; however, we can conclude that the chaotic nature of the system itself is sufficient to initiate the transitions. A possible approach for forecasting the transition events might be to compare multiple transients shortly before the transition occurs and to try to identify which similarities, if any, indicate the upcoming transition event.

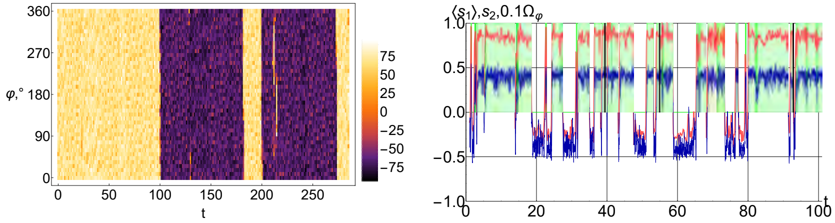

(a) (b)

Figure 15. Spatio-temporal diagram of the vertical velocity at $r = 1.5$ and $z = 0$ for $Ta = 2 \times 10^5$ (a). Comparison of calculated transient signals at $Ta = 5 \times 10^5$, where plotted in light red, green, and dark blue are a moving average of the flow angle from probes, $\langle s_1 \rangle$, the obtained binary signal from averaging the fluctuation energy of each attractor, s_2, and the mean azimuthal vorticity, $0.1\Omega_\varphi$, respectively (b).

3.3.2. Experimental results

The transient radial-to-azimuthal velocity ratio from the processed images of the observed angle of the dye stream are quite noisy (Fig. 18a,c). Thus, a moving average was calculated to complement the recorded signal. The experimental results show a long-lasting flow preference after $t \approx 33$. After this instant, all probes appear to indicate an outward radial jet in the upper half of the container. Prior to this instant, the preferred jet direction, although less conclusive, appears to be opposite, thus, indicating a regime change. The numerical results (Fig. 18b,d) show that the interval between switching events can exceed 50 dimensionless time units. Thus, the observation of only one switching event across the entire 22 h experiment is reasonable, albeit counter-intuitive result. Additionally, the experiment (Fig. 18a) and numerical calculation (Fig. 18b) results are in agreement that larger turbulent fluctuation relative to the mean signal is near the horizontal walls.

The statistical analysis of the experimentally detected short-lived transition intervals show that the plot slope follows $-3/2$ below $\tau = 0.05$, whereas the slope is steeper for larger τ (Fig. 17b). A possible explanation could be that some random noise was introduced during data processing, which produced false switching events. To reduce the effect of noise a moving average, $\langle s_1 \rangle$, was applied, which recovered the $-3/2$ slope.

No major disagreements were observed between numerical and experimental results. At the same time, a definitive evidence of regime change was not observed. The difficulty to ensure unperturbed conditions during such a long experiment is one of the main factors that may have contributed to this outcome. Additionally, the adverse influence of probes, as well as the heat from

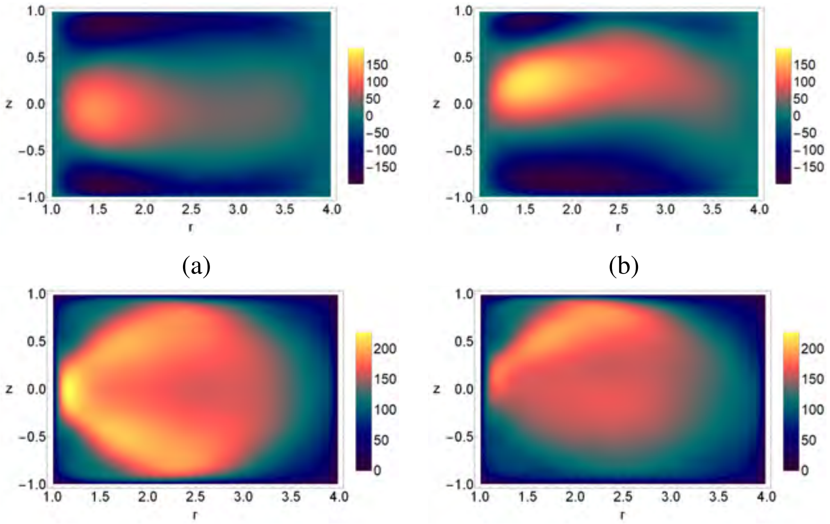

(a) (b)

(c) (d)

Figure 16. Time-averaged fields at $Ta = 10^6$. v_r averaged over: (a) all times; (b) only “up” attractor times. Velocity fluctuations averaged over: (c) all times; (d) only “up” attractor times.

the motor could not be excluded. A possible approach for the future studies could be to reduce the viscous time unit by choosing a smaller container. In such case, a more appropriate design choice would be a room-temperature liquid metal used in combination with UDV.

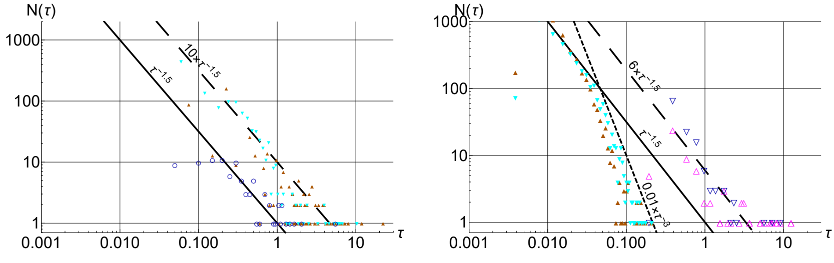

(a) (b)

Figure 17. Numerically calculated τ occurrences at $Ta = 2\times10^5$ and 3×10^5 and data of GRs plotted with filled upward triangles, filled downward triangles, and empty circles, respectively. The data were processed with parameter value $k = 5$ (a). Experimentally obtained τ occurrences at probe locations $\pm0.5h$ (upward triangles) and $\pm0.75h$ (downward triangles), where data have been sorted with s_1 (filled symbols) and $\langle s_1\rangle$ (empty symbols). The data were processed with parameter value $k = 1$ (b).

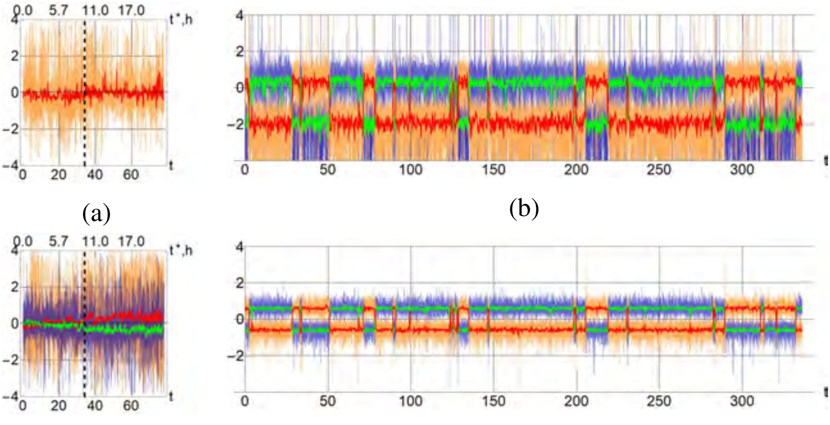

(a) (b)

(c) (d)

Figure 18. Experimental and numerical result comparison. Experimental results with magnet rotation frequency 70 rev/s corresponding to $Ta = 2.6\times10^5$ (a,c), where $t^* = th^2/\nu$ denotes the dimensional time. Numerical probe results at $Ta = 3\times10^5$ (b,d). Probe locations: (a) z=0.93h; (b) z=±0.93h; (c,d) z=±0.5h.

Conclusions

The derived analytical solution for electrically conducting cylinders and rings with a co-axially placed RPM can be used as a tool for quick visualizations of induced currents and volume force. Analytical form of the solution enables quick analysis over a range of geometrical parameters of the model. Furthermore, the analytical force solution was used to analytically express azimuthal velocity profile in shallow cylindrical containers and could potentially be used to further develop analytical solutions.

It was shown that the theory of RMF-induced turbulent flows in axisymmetric containers can be applied to RPM-induced flows providing the container aspect ratio ≈ 1. On the other hand, in shallow cylindrical containers with height-diameter ratio $\ll 1$, the distribution of body force affects the azimuthal velocity radial profile. By accounting for the force radial distribution in the theory, it was shown that the velocity maximum value is closer to the center of the cylindrical container near $r = r_o/2$. It is unlike for traditional RMF-induced flow, where the flow maximum is near the radial boundary. The numerically calculated and the experimentally measured azimuthal velocity radial profiles support this result. Numerical calculations showed that adding yokes at the poles of the magnet increases the axial magnetic flux near the ends of a cylindrical transversely magnetized PM and, thus, increases the effective magnet radius and stirring efficiency. The numerical results are supported by experimentally measured pressure at the container's radial boundary. Additionally, boundary layer solutions and numerical calculations showed that due to different magnitude and/or sign of the body force near the top and bottom boundaries, stirring the liquid metal in cylindrical container with a coaxial RPM from the bottom results in peak azimuthal velocity near the top boundary.

It was found that RPM generated flow stability in coaxial ring container decreases with increased ring outer radius until bistability phenomena occurs when outer to inner ring radius aspect ratios are above 3.2. Bistability phenomena implies the existence of multiple long-lived states and, thus, may be an explanation for the sometimes-poor performance of time-averaged turbulence modelling, which use the description of a single time-averaged state. The RPM-driven flow in the ring channel considered in this study exhibits turbulent bistability at a low Re, which allowed for extensive DNS studies. The two stable attractors in the studied setup manifested as the radially outward jet leaning towards the top or bottom of the container. The time-average – a vertically symmetric solution with the jet on the midplane – describes an unstable flow state. Thus, a turbulence model seeking the time-averaged flow is likely to encounter difficulties.

Moreover, the calculations showed that in the absence of external factors the chaotic nature of the system was sufficient to initiate a regime change.

The experimentally obtained temporal signal pattern showed a long-term flow preference, but bistability was not conclusively observed. Nevertheless, it was found that, characteristic for the on–off intermittency phenomena, the occurrence of time intervals between transitions followed the $-3/2$ slope in a log–log plot for both numerical and experimental data. In conclusion, the proposed system may serve as a convenient test case to further develop techniques aimed at prediction, identification, and description of the phenomenon.

Theses

1. Bistability phenomena may be an explanation for the sometimes-poor performance of time-averaged turbulence modelling. In the presence of two stable attractors, where the system can spend long intervals in each of them, the time-averaged state could be an unstable state. Thus, the time-averaged turbulence model, which seeks for a single time-averaged state, might encounter difficulty.
2. The proposed system for studying turbulent bistability – RPM-driven flow in the ring channel – exhibit the phenomena at low Reynolds numbers, thus, allowing for extensive DNS studies. As a result, this system may be used to further develop techniques aimed at prediction, identification, and description of the bistability phenomenon.
3. The derived analytical volume force solution can be a useful tool for parametric calculations of an RPM induced currents and volume force. The analytical form of currents enables further analytical development of related physical phenomena, as it was demonstrated by obtaining analytical solution for RPM-driven azimuthal velocity in cylindrical containers.

References

[1] P. A. Davidson. Swirling flow in an axisymmetric cavity of arbitrary profile, driven by a rotating magnetic field, *Journal of Fluid Mechanics* **245** (Dec. 1992), pp. 669–699. DOI: 10.1017/S0022112092000624.

[2] P. A. Davidson. Magnetohydrodynamics in materials processing, *Annual Review of Fluid Mechanics* **31**, no. 1 (1999), pp. 273–300. DOI: 10.1146/annurev.fluid.31.1.273.

[3] D. Vizman. “23 - Flow Control by Magnetic Fields during Crystal Growth from Melt”, *Handbook of Crystal Growth (Second Edition)*. Ed. by P. Rudolph. Second Edition. Handbook of Crystal Growth. Boston: Elsevier, 2015, pp. 909–950. ISBN: 978-0-444-63303-3. DOI: 10.1016/B978-0-444-63303-3.00023-7.

[4] I. Grants, V. Galindo, and G. Gerbeth. Linear and non-linear stability of melt flows in magnetic fields, *The European Physical Journal Special Topics* **220** (Mar. 2013), pp. 215–225. DOI: 10.1140/epjst/e2013-01809-0.

[5] P. Schwesig, M. Hainke, J. Friedrich, and G. Müller. Comparative numerical study of the effects of rotating and travelling magnetic fields on the interface shape and thermal stress in the VGF growth of InP crystals, *Journal of Crystal Growth* **266** (May 2004), pp. 224–228. DOI: 10.1016/j.jcrysgro.2004.02.049.

[6] I. Bucenieks. Perspectives of using rotating permanent magnets for electromagnetic induction pump design, *Magnetohydrodynamics* **36**, no. 2 (2000), pp. 151–156.

[7] I. Bucenieks. High pressure and high flowrate induction pumps with permanent magnets, *Magnetohydrodynamics* **39**, no. 4 (2003), pp. 411–418. DOI: 10.22364/mhd.39.4.4.

[8] I. Bucenieks. “Perspectives of Increasing Efficiency and Productivity of Electromagnetic Induction Pumps for Mercury Basing on Permanent Magnets”, *14th International Conference on Nuclear Engineering*. Vol. 2: Thermal Hydraulics. Miami, Florida, USA, Jan. 2006, pp. 185–189. DOI: 10.1115/ICONE14-89193.

[9] E. Koroteeva, M. Ščepanskis, I. Bucenieks, and E. Platacis. Numerical modeling and design of a disk-type rotating permanent magnet induction pump, *Fusion Engineering and Design* **106** (2016), pp. 85–92. ISSN: 0920-3796. DOI: 10.1016/j.fusengdes.2016.03.030.

[10] T. Beinerts, A. Bojarevičs, R. Baranovskis, M. Milgrāvis, and I. Kaldre. Permanent magnet dipole stirrer for aluminium furnaces, *IOP Conference Series: Materials Science and Engineering* **424** (Oct. 2018), p. 012037. DOI: 10.1088/1757-899X/424/1/012037.

[11] L. Goldsteins, I. Bucenieks, and L. Buligins. A simplified model of the centrifugal electromagnetic induction pump (CEMIP) with rotating permanent magnets, *Magnetohydrodynamics* **50**, no. 2 (2014), pp. 165–178. DOI: 10.22364/mhd.50.2.5.

[12] T. Beinerts, I. Bucenieks, A. Bojarevičs, and Y. Gelfgat. Possibility to use cylindrical pumps with permanent magnets in metallurgical facilities for aluminium alloys, *Magnetohydrodynamics* **51**, no. 4 (2015), pp. 757–770. DOI: 10.22364/mhd.51.4.9.

[13] P. A. Davidson, D. Kinnear, R. Lingwood, D. J. Short, and X. He. The role of Ekman pumping and the dominance of swirl in confined flows driven by Lorentz forces, *European Journal of Mechanics B-fluids - EUR J MECH B-FLUID* **18** (July 1999), pp. 693–711. DOI: 10.1016/S0997-7546(99)00106-5.

[14] V. Dzelme, M. Ščepanskis, V. Geža, A. Jakovičs, and M. Sarma. Modelling of liquid metal stirring induced by four counter-rotating permanent magnets, *Magnetohydrodynamics* **52**, no. 4 (2016), pp. 461–470. DOI: 10.22364/mhd.52.4.3.

[15] A. Gaile. “An Experimental Study of Electromagnetically Induced Liquid Metal Flow for Aluminium Transport and Degassing in a Linear Channel”. MA thesis. University of Latvia, 2021. URL: https://dspace.lu.lv/dspace/handle/7/55988.

[16] A. Bojarevičs, T. Beinerts, M. Sarma, and Y. Gelfgat. Arrays of Rotating Permanent Magnet Dipoles for Stirring and Pumping of Liquid Metals, *Journal for Manufacturing Science and Production* **15**, no. 1 (2015), pp. 35–39. DOI: 10.1515/jmsp-2014-0039.

[17] A. Caciagli, R. Baars, A. Philipse, and B. W.M. Kuipers. Exact expression for the magnetic field of a finite cylinder with arbitrary uniform magnetization, *Journal of Magnetism and Magnetic Materials* **456** (June 2018), pp. 423–432. DOI: 10.1016/j.jmmm.2018.02.003.

[18] L. P. Gorbachev, N. V. Nikitin, and A. L. Ustinov. Magnetohydrodynamic rotation of electrically conducting liquid in a cylindrical vessel of finite dimensions, *Magnetohydrodynamics* **10**, no. 4 (1974), pp. 406–414.

[19] J. Stiller, K. Koal, and R. Grundmann. “Stirring of melts using rotating and travelling magnetic fields”, *Fifth International Conference on CFD in the Process Industries.* CSIRO, Melbourne, Australia, Dec. 2006.

[20] I. Grants, C. Zhang, S. Eckert, and G. Gerbeth. Experimental observation of swirl accumulation in a magnetically driven flow, *Journal of Fluid Mechanics* **616** (Dec. 2008), pp. 135–152. DOI: 10.1017/S0022112008003650.

[21] Yu. M. Gelfgat and A. Gelfgat. Experimental and numerical study of rotating magnetic field driven flow in cylindrical enclosures with different aspect ratios, *Magnetohydrodynamics* **40**, no. 2 (2004), pp. 147–160. DOI: 10.22364/mhd.40.2.3.

[22] M. Rivero, S. Cuevas, and E. Ramos. Magnetohydrodynamic flow induced by arrays of rotating permanent magnets, *Experimental Thermal and Fluid Science* **78** (2016), pp. 30–40. ISSN: 0894-1777. DOI: 10.1016/j.expthermflusci.2016.05.008.

[23] A. Morev and A. Aliferov. Study of an aluminium mixing system based on permanent magnets, *The international journal for computation and mathematics in electrical and electronic engineering* **39** (2020), pp. 192–197. ISSN: 0332-1649. DOI: 10.1108/COMPEL-06-2019-0233.

[24] I. Grants, G. Gerbeth, and A. Bojarevičs. Contactless magnetic excitation of acoustic cavitation in liquid metals, *Journal of Applied Physics* **117** (2015). 204901. DOI: 10.1063/1.4921164.

[25] I. Kaldre, A. Bojarevičs, I. Grants, T. Beinerts, M. Kalvāns, M. Milgrāvis, and G. Gerbeth. Nanoparticle dispersion in liquid metals by electromagnetically induced acoustic cavitation, *Acta Materialia* **118** (2016), pp. 253–259. DOI: 10.1016/j.actamat.2016.07.045.

[26] M. Kalvāns, A. Bojarevičs, I. Kaldre, and T. Beinerts. “Assessment of Linear Permanent Magnet Liquid Metal Dispenser”, 2016.

[27] I. Kaldre, M. Milgravis, A. Bojarevics, and T. Beinerts. Electromagnetic Processing during Directional Solidification of Particle-Strengthened Aluminum Alloys for Additive Manufacturing, *Materials Proceedings* **3**, no. 1 (2021). ISSN: 2673-4605. DOI: 10.3390/IEC2M-09255.

[28] M. Milgrāvis, G. Kroŋkalns, R. Nikoluškins, T. Beinerts, M. Kalvāns, A. Bojarevičs, and I. A. Perianu. Electromagnetic Methods for Production of Aluminium Metal Matrix Composites, *Solid State Phenomena* **332** (June 2022), pp. 19–27. DOI: 10.4028/p-9shcqm.

[29] G. Lopez-Santana, A. Kennaugh, and A. Keshmiri. Experimental Techniques against RANS Method in a Fully Developed Turbulent Pipe Flow: Evolution of Experimental and Computational Methods for the Study of Turbulence, *Fluids* **7**, no. 2 (2022). ISSN: 2311-5521. DOI: 10.3390/fluids7020078.

[30] S. Vijiapurapu and J. Cui. Performance of turbulence models for flows through rough pipes, *Applied Mathematical Modelling* **34**, no. 6 (2010), pp. 1458–1466. ISSN: 0307-904X. DOI: 10.1016/j.apm.2009.08.029.

[31] A. Gupta and R. Kumar. Three-dimensional turbulent swirling flow in a cylinder: Experiments and computations, *International Journal of Heat and Fluid Flow* **28**, no. 2 (2007), pp. 249–261. ISSN: 0142-727X. DOI: 10.1016/j.ijheatfluidflow.2006.04.005.

[32] N. N. Zadeh and R. Paoli. Numerical Experiments of Subsonic Jet Flow Simulations Using RANS with OpenFOAM, *Open Journal of Fluid Dynamics* **12** (2022), pp. 230–247. DOI: 10.4236/ojfd.2022.122011.

[33] M. Breuer, D. Lakehal, and W. Rodi. “Flow around a Surface Mounted Cubical Obstacle: Comparison of Les and Rans-Results”, *Computation of Three-Dimensional Complex Flows: Proceedings of the IMACS-COST Conference on Computational Fluid Dynamics Lausanne, September 13–15, 1995.* Ed. by M. Deville, S. Gavrilakis, and I. L. Ryhming. Wiesbaden: Vieweg+Teubner Verlag, 1996, pp. 22–30. ISBN: 978-3-322-89838-8. DOI: 10.1007/978-3-322-89838-8_4.

[34] Z. Xie and I. P. Castro. LES and RANS for Turbulent Flow over Arrays of Wall-Mounted Obstacles, *Flow, Turbulence and Combustion* **76**, no. 3 (Apr. 2006), pp. 291–312. ISSN: 1573-1987. DOI: 10.1007/s10494-006-9018-6.

[35] Y. Velísková, Z. Chára, R. Schügerl, and R. Dulovičová. CFD simulation of flow behind overflooded obstacle, *Journal of Hydrology and Hydromechanics* **66**, no. 4 (2018), pp. 448–456. DOI: 10.2478/johh-2018-0028.

[36] E. Hopf. A mathematical example displaying features of turbulence, *Communications on Pure and Applied Mathematics* **1**, no. 4 (1948), pp. 303–322. DOI: 10.1002/cpa.3160010401.

[37] L. Larger, J.-P. Goedgebuer, and T. Erneux. Subcritical Hopf bifurcation in dynamical systems described by a scalar nonlinear delay differential equation, *Phys. Rev. E* **69** (3 Mar. 2004), p. 036210. DOI: 10.1103/PhysRevE.69.036210.

[38] Y. Pomeau and P. Manneville. Intermittent transition to turbulence in dissipative dynamical systems, *Communications in Mathematical Physics* **74**, no. 2 (1980), pp. 189–197. DOI: 10.1007/BF01197757.

[39] A. E. Hramov, A. A. Koronovskii, M. K. Kurovskaya, and S. Boccaletti. Ring Intermittency in Coupled Chaotic Oscillators at the Boundary of Phase Synchronization, *Phys. Rev. Lett.* **97** (11 Sept. 2006), p. 114101. DOI: 10.1103/PhysRevLett.97.114101.

[40] G. Dong, L. Tian, J. Xia, S. Zheng, and R. Du. Sudden occurrence of chaos-II in nonsmooth maps, *International Journal of Bifurcation and Chaos* **20**, no. 12 (2010), pp. 4159–4174. DOI: 10.1142/S0218127410028276.

[41] A. E. Hramov, A. A. Koronovskii, M. K. Kurovskaya, and O. I. Moskalenko. Type-I intermittency with noise versus eyelet intermittency, *Physics Letters A* **375**, no. 15 (2011), pp. 1646–1652. ISSN: 0375-9601. DOI: 10.1016/j.physleta.2011.02.032.

[42] N. Platt, E. A. Spiegel, and C. Tresser. On-off intermittency: A mechanism for bursting, *Phys. Rev. Lett.* **70** (3 Jan. 1993), pp. 279–282. DOI: 10.1103/PhysRevLett.70.279.

[43] Y.-C. Lai and C. Grebogi. Intermingled basins and two-state on-off intermittency, *Phys. Rev. E* **52** (4 Oct. 1995), R3313–R3316. DOI: 10.1103/PhysRevE.52.R3313.

[44] J. F. Heagy, N. Platt, and S. M. Hammel. Characterization of on-off intermittency, *Phys. Rev. E* **49** (2 Feb. 1994), pp. 1140–1150. DOI: 10.1103/PhysRevE.49.1140.

[45] A. E. Hramov, A. A. Koronovskii, I. S. Midzyanovskaya, E. Sitnikova, and C. M. van Rijn. On-off intermittency in time series of spontaneous paroxysmal activity in rats with genetic absence epilepsy, *Chaos: An Interdisciplinary Journal of Nonlinear Science* **16**, no. 4 (2006), p. 043111. DOI: 10.1063/1.2360505.

[46] Z. Qian, C. Zeng-Qiang, and Y. Zhu-Zhi. Generation of on–off intermittency based on Rössler chaotic system, *Chinese Physics* **16**, no. 9 (Sept. 2007), pp. 2616–2626. DOI: 10.1088/1009-1963/16/9/020.

[47] M. Grandemange, M. Gohlke, and O. Cadot. Bi-stability in the turbulent wake past parallelepiped bodies with various aspect ratios and wall effects, *Physics of Fluids* **25**, no. 9 (2013), p. 095103. DOI: 10.1063/1.4820372.

[48] Y. Fan, C. Xia, S. Chu, Z. Yang, and O. Cadot. Experimental and numerical analysis of the bi-stable turbulent wake of a rectangular flat-backed bluff body, *Physics of Fluids* **32**, no. 10 (2020), p. 105111. DOI: 10.1063/5.0019794.

[49] K. He, G. Minelli, X. Su, G. Gao, and S. Krajnović. On state instability of the bi-stable flow past a notchback bluff body, *Journal of Fluid Mechanics* **931** (2022), R6. DOI: 10.1017/jfm.2021.1025.

[50] N. Deng, B. R. Noack, M. Morzyński, and L. R. Pastur. Low-order model for successive bifurcations of the fluidic pinball, *Journal of Fluid Mechanics* **884** (2020), A37. DOI: 10.1017/jfm.2019.959.

[51] P. P. Galuzio, S. R. Lopes, and R. L. Viana. Two-State On-Off Intermittency and the Onset of Turbulence in a Spatiotemporally Chaotic System, *Phys. Rev. Lett.* **105** (5 July 2010), p. 055001. DOI: 10.1103/PhysRevLett.105.055001.

[52] F. Garcia, M. Seilmayer, A. Giesecke, and F. Stefani. Intermittent chaotic flows in the weakly magnetised spherical Couette system, *PAMM* **21**, no. 1 (2021), e202100024. DOI: 10.1002/pamm.202100024.

[53] I. A. Belyaev, D. A. Biryukov, D. N. Gerasimov, and E. I. Yurin. On-off intermittency and hard turbulence in the flow of fluid in the magnetic field, *Chaos: An Interdisciplinary Journal of Nonlinear Science* **29**, no. 8 (2019), p. 083119. DOI: 10.1063/1.5098538.

[54] J. L. Cabrera and J. G. Milton. On-Off Intermittency in a Human Balancing Task, *Phys. Rev. Lett.* **89** (15 Sept. 2002), p. 158702. DOI: 10.1103/PhysRevLett.89.158702.

[55] S. C. Cande and D. V. Kent. Revised calibration of the geomagnetic polarity timescale for the Late Cretaceous and Cenozoic, *Journal of Geophysical Research: Solid Earth* **100**, no. B4 (1995), pp. 6093–6095. DOI: 10.1029/94JB03098.

[56] P. Ashwin, A. M. Rucklidge, and R. Sturman. Two-state intermittency near a symmetric interaction of saddle-node and Hopf bifurcations: a case study from dynamo theory, *Physica D: Nonlinear Phenomena* **194**, no. 1 (2004), pp. 30–48. ISSN: 0167-2789. DOI: 10.1016/j.physd.2004.02.002.

[57] A. Yu. Kurazhkovskii, N. A. Kurazhkovskaya, and B. I. Klain. Stochastic behavior of geomagnetic field in the Middle Jurassic-Paleogene, *Geomagnetism and Aeronomy* **55** (2 2015), pp. 223–234. ISSN: 1555-645X. DOI: 10.1134/S0016793215010089.

[58] M. Landeau, A. Fournier, H.-C. Nataf, D. Cébron, and N. Schaeffer. Sustaining Earth's magnetic dynamo, *Nature Reviews Earth & Environment* **3**, no. 4 (Apr. 2022), pp. 255–269. ISSN: 2662-138X. DOI: 10.1038/s43017-022-00264-1.

[59] F. Lepreti, V. Carbone, P. Giuliani, L. Sorriso–Valvo, and P. Veltri. Statistical properties of dissipation bursts within turbulence: Solar flares and geomagnetic activity, *Planetary and Space Science* **52**, no. 10 (2004). Nonlinear Processes in Solar System Plasmas, pp. 957–962. ISSN: 0032-0633. DOI: 10.1016/j.pss.2004.03.001.

[60] N. Platt, E. A. Spiegel, and C. Tresser. The intermittent solar cycle, *Geophysical & Astrophysical Fluid Dynamics* **73**, no. 1-4 (1993), pp. 147–161. DOI: 10.1080/03091929308203626.

[61] F. Stefani, J. Beer, A. Giesecke, T. Gloaguen, M. Seilmayer, R. Stepanov, and T. Weier. Phase coherence and phase jumps in the Schwabe cycle, *Astronomische Nachrichten* **341**, no. 6-7 (2020), pp. 600–615. DOI: 10.1002/asna.202013809.

[62] H.-C. Nataf. Tidally Synchronized Solar Dynamo: A Rebuttal, *Solar Physics* **297**, no. 8 (Aug. 2022), p. 107. ISSN: 1573-093X. DOI: 10.1007/s11207-022-02038-w.

[63] J. Vencels, P. Råback, and V. Geža. EOF-Library: Open-source Elmer FEM and OpenFOAM coupler for electromagnetics and fluid dynamics, *SoftwareX* **9** (2019), pp. 68–72. ISSN: 2352-7110. DOI: 10.1016/j.softx.2019.01.007.

[64] D. J. Griffiths. *Introduction to electrodynamics. 3rd Edition.* London: Prentice-Hall, 1999. Chap. 7.1 and 10.1.

[65] A. Bojarevičs and T. Beinerts. Experiments on liquid metal flow induced by a rotating magnetic dipole, *Magnetohydrodynamics* **46**, no. 4 (2010), pp. 333–338. DOI: 10.22364/mhd.46.4.2.

[66] P. Spalart and S. Allmaras. A one-equation turbulence model for aerodynamic flows, *Recherche Aerospatiale* no. 1 (1994), pp. 5–21.

[67] I. Grants and D. Berenis. Stability of electrically conducting liquid flow driven by a rotating magnetic dipole in a ring channel, *Physics of Fluids* **32**, no. 4 (2020), p. 044104. DOI: 10.1063/5.0002094.

[68] W.M. Haynes. *CRC Handbook of Chemistry and Physics.* CRC Press, 2016. ISBN: 9781498754293.

[69] G. Gritzner and R. F. Phillips. Densities, viscosities, and vapor pressures of copper(II) chloride solutions in hydrochloric acid, *Journal of Chemical & Engineering Data* **17**, no. 4 (1972), pp. 425–428. DOI: 10.1021/je60055a006.

[70] C. Steger. An unbiased detector of curvilinear structures, *IEEE Transactions on Pattern Analysis and Machine Intelligence* **20**, no. 2 (1998), pp. 113–125. DOI: 10.1109/34.659930.

[71] T. Wagner, M. Hiner, and X. Raynaud. thorstenwagner/ij-ridgedetection: Ridge Detection 1.4.0. Version v1.4.0, (Aug. 2017). DOI: 10.5281/zenodo.845874.